
Instability in Diffusion ODEs: An Explanation for Inaccurate Image Reconstruction

Han Zhang^{1*‡} Jinghong Mao* Shangwen Zhu¹ Zhantao Yang^{1‡}
Lianghua Huang² Yu Liu² Deli Zhao³ Ruili Feng² Fan Cheng^{1†}

¹Shanghai Jiao Tong University ²Tongyi Lab ³Alibaba Group

Abstract

Diffusion reconstruction plays a critical role in various applications such as image editing, restoration, and style transfer. In theory, the reconstruction should be simple – it just inverts and regenerates images by numerically solving the Probability-Flow Ordinary Differential Equation (PF-ODE). Yet in practice, noticeable reconstruction errors have been observed, which cannot be well explained by numerical errors. In this work, we identify a deeper intrinsic property in the PF-ODE generation process, the *instability*, that can further amplify the reconstruction errors. The root of this instability lies in *the sparsity inherent in the generation distribution, which means that the probability is concentrated on scattered and small regions while the vast majority remains almost empty*. To demonstrate the existence of instability and its amplification on reconstruction error, we conduct experiments on both toy numerical examples and popular open-sourced diffusion models. Furthermore, based on the characteristics of image data, we theoretically prove that the instability’s probability converges to one as the data dimensionality increases. Our findings highlight the inherent challenges in diffusion-based reconstruction and can offer insights for future improvements.

1 Introduction

Diffusion models have rapidly emerged as a pivotal class of generative models, demonstrating superior performance, particularly in image generation [18, 37, 38, 36, 3, 34, 33, 35, 23, 24, 11, 29]. A fundamental technique within diffusion models is diffusion reconstruction, which comprises diffusion inversion [40, 36, 7] and diffusion generation—both executed through numerical solving the Probability Flow Ordinary Differential Equations (PF-ODEs) [41, 30]. Diffusion inversion¹ first converts an image into an inverted noise, which is then used by diffusion generation process to reconstruct the original image. Diffusion reconstruction is crucial due to its extensive applications in downstream tasks, including image editing [15, 16], restoration [50], and style transfer [43].

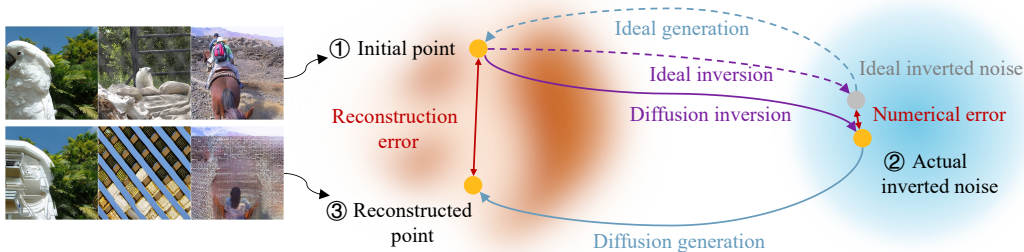
From the theoretical perspective, the reconstruction should be simple, which only needs to numerically solve the PF-ODE in two opposite directions. Yet in practice, significant reconstruction errors can occasionally happen, as shown in Figure 1. Although previous works attribute the reconstruction inaccuracies to the inherent numerical discretization errors in solving PF-ODEs [47, 48, 25, 51], it does not well explain such significant discrepancy. The fundamental causes underlying these pronounced reconstruction discrepancies remain systematically unexplored.

In this work, we point out the existence of *instability* in the diffusion generation process, and demonstrate its amplification effect on the reconstruction errors. Specifically, instability characterizes

*Equal contribution. ‡Work performed during internship at Tongyi Lab. †Corresponding author.

Emails: Han Zhang <hzhang9617@gmail.com>, Jinghong Mao <maojh1009@gmail.com>, Fan Cheng <chengfan@sjtu.edu.cn>.

¹We follow the convention that uses *inversion* indicating solving PF-ODE along the forward time [32, 47, 51].



Original and reconstructed images Data Distribution Gaussian
Figure 1: Instability amplifies diffusion reconstruction errors. Given an *initial point* in the *data inverted noise*, the reconstruction process first undergoes *diffusion inversion* to produce the *actual inverted noise*. *Numerical errors* introduced by the inversion will cause the actual inverted noise to deviate from the theoretically ideal inverted noise. When the generation process exhibits instability, these numerical errors are amplified, resulting in significantly larger *reconstruction errors*. This amplification makes accurate reconstruction challenging.

scenarios where the diffusion generation process is sensitive to the initial noise. Thus, any numerical error in the inverted noise will be amplified during the regeneration phase. Figure 1 illustrates the process by which reconstruction errors arise.

To further demonstrate the presence of instability from a theoretical perspective, we establish a lower bound on the probability of instability. Note that here we choose to analyze the ideal diffusion reconstruction process, which is free from the influence of any numerical error and focused on the inherent property of PF-ODE. Based on reasonable assumptions about the real image distribution and the generation distribution of diffusion models, we demonstrate that when the data dimensionality increases as infinity, the probability of instability in reconstruction tends to one! Considering the high dimensionality of image data, such surprising asymptotic result provides theoretical justification for the instability observed in image reconstruction within diffusion models.

Mechanisms of instability. For better understanding on the mechanism behind the instability in diffusion reconstruction, we provide an intuitive illustration in Figure 2. Our analysis reveals that *the sparsity of the generation distribution plays a pivotal role in the emergence of instability*. Here, the sparsity means that the generation distribution is concentrated in scattered, small regions, while the majority of regions possess low probability density. Recall that the PF-ODE-based generation process actually builds a push-forward mapping from the Gaussian distribution to generation distribution. According to the push-forward formula, the generation mapping must preserve probability. Thus, *suppose a region A in the Gaussian distribution is mapped to a significantly lower density region B in the generation distribution, the area of region B will be extended to maintain the probability*. This expansion necessitates large gradients in the generation process, indicating the emergence of instability. Meanwhile, during image reconstruction, the initial image is sampled from some underlying real distribution. This real distribution is generally different from the generation distribution. Such distribution discrepancy can lead to a non-negligible probability that the initial image resides in the low density region of the generation distribution, and thus make the instability high probable.

Main organization. In Section 2, we will introduce preliminaries about PF-ODE and the definition of instability. Subsequently in Section 3, we will provide experimental evidence that instability actually exists in diffusion generation, and then demonstrate its amplification on reconstruction error. Finally in Section 4, we further provide theoretical evidence on instability. Based on the characteristics of image distributions, we reveal that the sparsity of generation distribution can induce the instability, and theoretically prove that the instability will almost surely occur during reconstruction for infinite dimensional images.

2 Preliminaries

2.1 Diffusion models and probability flow ODE

Diffusion models can generate samples under desired distribution π_{gen} from noise under standard Gaussian distribution $\mathcal{N}(\mathbf{0}, \mathbf{I})$ [18, 41]. The generation process can be achieved by numerically

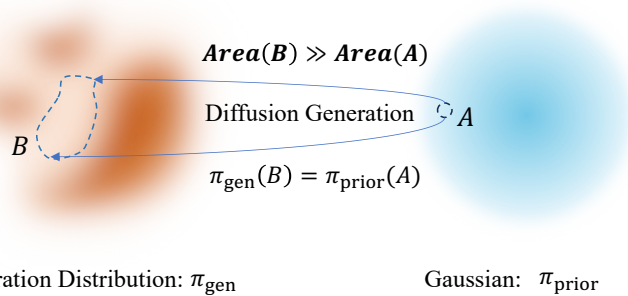


Figure 2: **Intuitive illustration of instability occurrence during the generation process.** For typical image data, the generation distribution is inherently sparse, meaning that most of the probability mass is concentrated in scattered, small regions, while the majority of the space has low probability. In contrast, the prior distribution for the generation process, *i.e.*, the Gaussian, concentrates its probability within a bounded region and is relatively uniformly distributed. According to the push-forward formula, the generation mapping must preserve probability measures, ensuring that the image of a probability region A under the generation mapping B satisfies $\pi_{\text{gen}}(B) = \pi_{\text{prior}}(A)$. When B falls into a low-density region of the generation distribution, significantly lower than the density at A , maintaining probability equality requires that the area (or more rigorously, the Lebesgue measure) of B be much larger than that of A . This amplification effect results in large gradients during the generation process, indicating the emergence of instability. The probability of the instability is analyzed in Section 4 in detail.

solving the PF-ODE [2, 41, 28]:

$$d\mathbf{x}_t/dt = \mathbf{v}(\mathbf{x}_t, t), \text{ where } \mathbf{v}(\mathbf{x}, t) = \mathbb{E}[Z - X|X_t = \mathbf{x}], \quad (1)$$

$t \in [0, 1]$, $\mathbf{v} : \mathbb{R}^n \times [0, 1] \rightarrow \mathbb{R}^n$ is a time-dependent vector field defined by the conditional expectation in Equation (1). In the expectation, the noise $Z \sim \mathcal{N}(\mathbf{0}, \mathbf{I})$ and the data $X \sim \pi_{\text{gen}}$ are independently sampled, $X_t = (1 - t)X + tZ$ is a linear interpolation between them.

Note that here we adopt the flow matching formulation to represent the PF-ODE [28, 27], and the subsequent sections will consistently utilize this formulation. Here, we adopt the flow matching formulation for two reasons: 1) the flow matching formulation is actually equivalent to conventional PF-ODEs when one distribution is set to Gaussian [41, 28, 1], and 2) this formulation is widely adopted in recent top-tier text-to-image models [11, 5].

Diffusion generation and inversion. Both diffusion generation and inversion solve the PF-ODE in Equation (1), but in opposite directions. Diffusion generation mapping can produce data samples from initial noise, while diffusion inversion mapping yields an inverted noise from an initial data. We formally define these two mappings as follows:

Definition 2.1 (Diffusion generation and inversion mappings). The diffusion generation mapping $G : \mathbb{R}^n \rightarrow \text{supp}(\pi_{\text{gen}})$ is defined as $G(\mathbf{z}) = \mathbf{x}_0$, where \mathbf{x}_0 is the solution at $t = 0$ of the ODE Equation (1) with the initial value $\mathbf{x}_1 = \mathbf{z}$ at $t = 1$. Meanwhile, the diffusion inversion mapping can be denoted by G^{-1} , the inverse function of the generation mapping.

2.2 Definition of instability

For later analysis, we first provide the definition of Intrinsic instability for general mapping F .

Definition 2.2 (Intrinsic instability). Suppose $F : \mathbb{R}^n \rightarrow \mathbb{R}^n$ is a continuously differentiable mapping. For an input vector $\mathbf{x} \in \mathbb{R}^n$, if there exists another non-zero vector $\mathbf{u} \in \mathbb{R}^n$ such that

$$\mathcal{E}_F(\mathbf{x}, \mathbf{u}) := \|J_F(\mathbf{x})\mathbf{u}\| / \|\mathbf{u}\| > 1, \quad (2)$$

where $J_F(\mathbf{x}) \in \mathbb{R}^{n \times n}$ denotes the Jacobian matrix of F evaluated at \mathbf{x} , then we say that F exhibits the *intrinsic instability* at \mathbf{x} in the direction \mathbf{u} . The scalar $\mathcal{E}_F(\mathbf{x}, \mathbf{u})$ is referred to as the *intrinsic instability coefficient* of F at \mathbf{x} along the direction \mathbf{u} .

When the intrinsic instability coefficient exceeding one, it indeed indicates that the mapping F amplifies any *infinitesimal perturbation* along the specific direction \mathbf{u} . The magnitude of $\mathcal{E}_F(\mathbf{x}, \mathbf{u})$ quantitatively measures the sensitivity of F to changes in the input direction \mathbf{u} . The following

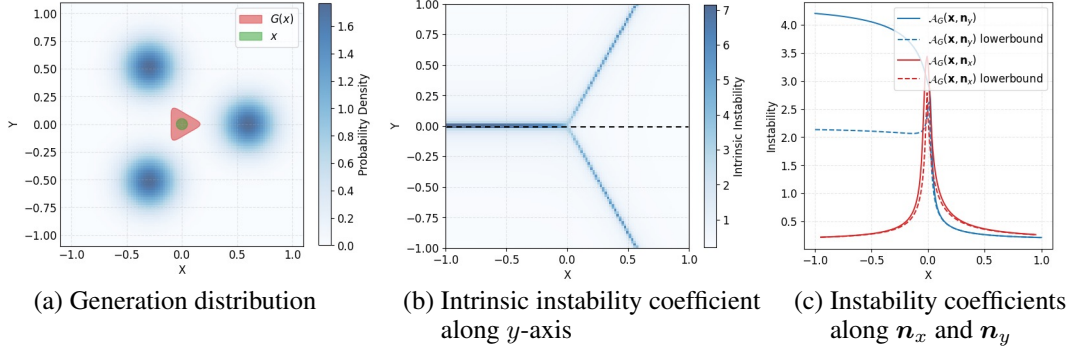


Figure 3: **Experimental evidence on the existence of instability for a two-dimensional generation distribution.** (a) visualizes the density function of the generation distribution, which is a mixture of Gaussians generated from a standard gaussian. The green region, after applying generation mapping, becomes a significantly larger red region. (b) visualizes the intrinsic instability coefficient along the y -axis. It is observed that the intrinsic instability coefficient along the y -axis in the central region significantly exceeds one, consistent with the position of the green region in (a). For each point on the dashed line in (b), we compute the instability coefficient $\mathcal{A}_G(\mathbf{x}, \mathbf{n})$ of diffusion generation mapping G under perturbation \mathbf{n}_x along x -axis and perturbation \mathbf{n}_y along y -axis, respectively. The results are shown in (c). The dashed lines show the lower bounds of $\mathcal{A}_G(\mathbf{x}, \mathbf{n})$ given in Proposition 2.1.

proposition will better illustrate this error amplification phenomenon for *non-negligible perturbations*, which we refer to as *instability effect*, when intrinsic instability occurs:

Proposition 2.1 (Instability effect). *Suppose $F : \mathbb{R}^n \rightarrow \mathbb{R}^n$ is a continuously differentiable mapping. For any $\mathbf{x}, \mathbf{u} \in \mathbb{R}^n$, and any $\Delta > 0$, there exists a non-zero perturbation $\mathbf{n} \in \mathbb{R}^n$ such that*

$$\mathcal{A}_F(\mathbf{x}, \mathbf{n}) := \frac{\|F(\mathbf{x} + \mathbf{n}) - F(\mathbf{x})\|}{\|\mathbf{n}\|} \geq \frac{\mathcal{E}_F(\mathbf{x}, \mathbf{u})}{1 + \Delta}, \quad (3)$$

where $\mathcal{A}_F(\mathbf{x}, \mathbf{n})$ is referred to as the instability coefficient. Furthermore, if $\mathcal{E}_F(\mathbf{x}, \mathbf{u}) > 1$, we have a \mathbf{n} that satisfies $\mathcal{A}_F(\mathbf{x}, \mathbf{n}) > 1$, then we say that F exhibits the instability at \mathbf{x} under perturbation \mathbf{n} .

3 Instability and its amplification on reconstruction error

In this section, we first empirically demonstrate the existence of instability in the diffusion generation mapping G in Section 3.1. Subsequently, we present experimental evidence corroborating the positive correlation between instability and the reconstruction error in Section 3.2.

3.1 Empirical evidence on the existence of instability

In Section 2.2, we have defined the intrinsic instability and introduced the instability effect. Here, we will demonstrate that the instability can exist in the generation process of diffusion models.

Demonstration by a numerical case. We present a numerical example illustrated in Figure 3. The density function of the diffusion generation distribution is depicted in Figure 3(a). The detailed settings are provided in the supplementary material.

In Figure 3(a), the red region is obtained by applying the diffusion generation mapping G to the green region. It is evident that G significantly expands the green region along the y -axis, indicating that G is highly sensitive to perturbations along the y -axis within the green region. Figure 3(b) displays the intrinsic instability coefficient of G along the y -axis. It can be observed that the intrinsic instability coefficient along the y -axis exceeds one in the central region, indicating that the instability effect can appear in this area. Moreover, this region coincides with the green region in Figure 3(a), demonstrating the relationship between the intrinsic instability and the amplification effect.

We further analyze the instability coefficient $\mathcal{A}_G(\mathbf{x}, \mathbf{n})$ along the dashed line in Figure 3(b), as well as the lower bound provided by Proposition 2.1. The curves of $\mathcal{A}_G(\mathbf{x}, \mathbf{n})$ vs. x are shown in Figure 3(c). We observe that in the central region, the instability coefficients along x and y axis, i.e., $\mathcal{A}_G(\mathbf{x}, \mathbf{n}_x)$ and $\mathcal{A}_G(\mathbf{x}, \mathbf{n}_y)$, are greater than one, further indicating the presence of instability.

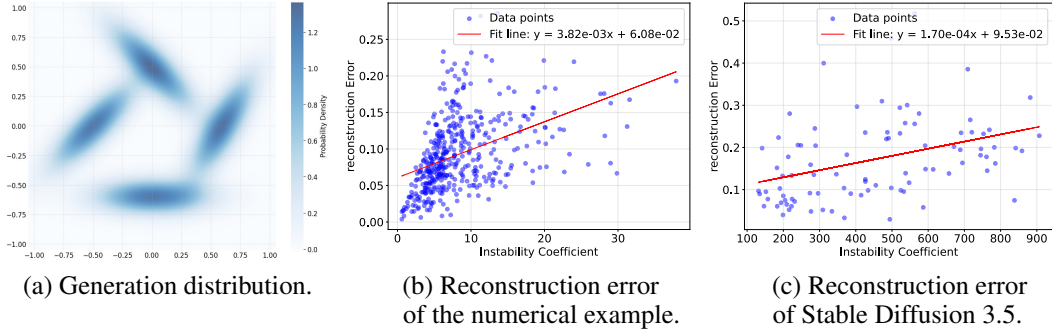


Figure 4: **Positive correlation between the reconstruction error and instability coefficient in a numerical case and Stable Diffusion 3.5 [11].** In numerical experiments, the diffusion model’s generation distribution is a two-dimensional mixture of Gaussians. (a) shows the probability density function. (b) displays the relationship between reconstruction error $\mathcal{R}(\mathbf{x})$ and instability coefficient obtained from reconstruction of different initial values \mathbf{x} . (c) further illustrates the relationship between reconstruction error and instability coefficient in the Stable Diffusion 3.5 model.

3.2 Instability amplifies reconstruction error

This subsection demonstrates that instability in diffusion generation can amplify reconstruction errors. We begin by formally defining the reconstruction error, and provide a theoretical support on the possibility of large reconstruction error. Then we demonstrate the amplification effect by correlation analyses using both numerical cases and practical diffusion models.

Reconstruction error. Diffusion reconstruction involves two primary steps for a given data $\mathbf{x} \in \mathbb{R}^n$:

1. The diffusion inversion process defined by Definition 2.1 is numerically solved from the given data \mathbf{x} , which yields an inverted noise $\hat{\mathbf{z}} = \hat{G}^{-1}(\mathbf{x})$; and then
2. the diffusion generation process defined by Equation (1) is numerically solved from $\hat{\mathbf{z}}$, resulting in a reconstructed data $\hat{\mathbf{x}} = \hat{G}(\hat{\mathbf{z}})$,

where \hat{G} denotes the approximated diffusion generation mapping by numerically solving PF-ODE in Equation (1), and \hat{G}^{-1} denotes the approximated diffusion inversion mapping, similarly.

The reconstruction error is quantified as the discrepancy between the original data \mathbf{x} and the reconstructed data $\hat{\mathbf{x}}$. It can be defined as:

$$\mathcal{R}(\mathbf{x}) = \frac{1}{\sqrt{n}} \|\mathbf{x} - \hat{\mathbf{x}}\|_2 = \frac{1}{\sqrt{n}} \|\mathbf{x} - \hat{G}(\hat{\mathbf{z}})\|_2 = \frac{1}{\sqrt{n}} \|\mathbf{x} - \hat{G}(\hat{G}^{-1}(\mathbf{x}))\|_2. \quad (4)$$

To analyze the causes of reconstruction error, it is essential to recognize two primary factors:

1. *Discrepancy in inverted noise:* The inverted noise $\hat{\mathbf{z}} = \hat{G}^{-1}(\mathbf{x})$ obtained during the diffusion inversion process deviates from the ideal noise $\mathbf{z} \sim \mathcal{N}(\mathbf{0}, \mathbf{I})$. This discrepancy arises due to numerical discretization errors inherent in solving the PF-ODE Equation (1) and its inverse. As a result, the numerically inverted noise does not perfectly match the ideal one, introducing an initial error into the regeneration pipeline.
2. *Amplification by instability:* The presence of instability in the diffusion generation mapping \hat{G} can further exacerbate the above discrepancy in the inverted noise, leading to a substantial reconstruction error $\mathcal{R}(\mathbf{x})$.

The following theorem further demonstrates that both of the aforementioned two factors contribute to the reconstruction error, even if the diffusion generation mapping G is ideal with infinite numerical precision. A detailed proof is provided in the supplementary material.

Theorem 3.1 (Risk of large reconstruction error). *For any data sample $\mathbf{x} \in \mathbb{R}^n$, consider the diffusion reconstruction process consisting of a numerically approximated diffusion inversion under Euler method and a precise diffusion generation process G . Let $\hat{\mathbf{z}}$ denote the numerically inverted noise, \mathbf{z} denote the ideal inverted noise, and $\hat{\mathbf{x}}$ denote the reconstructed data. Suppose $\mathcal{E}_G(\mathbf{z}', \hat{\mathbf{z}} - \mathbf{z}) > C$ for some $C > 0$ and all $\mathbf{z}' \in \{t\mathbf{z} + (1-t)\hat{\mathbf{z}} : t \in [0, 1]\}$. Then, the upper bound \mathcal{U} of reconstruction*

error $\mathcal{R}(\mathbf{x})$ satisfies:

$$\mathcal{U} \geq \underbrace{hM_2 \frac{(C-1)}{2 \log C}}_{\text{Numerical error in inverted noise}} \cdot \underbrace{C}_{\text{Instability amplification}}, \quad (5)$$

where h represents the step size in the numerical solution, and M_2 is the estimated upper bound term for the local truncation error of the Euler method.

A numerical case. To verify the amplification effect of instability on reconstruction error, we conduct numerical experiments on a diffusion model with a simple generation distribution. Then, we analyze the correlation between the reconstruction error and the instability coefficient. The density function of the generation distribution is illustrated in Figure 4(a). Detailed settings are provided in the supplementary material.

The experimental results are presented in Figure 4(b). We observe a significant correlation between the reconstruction error $\mathcal{R}(\mathbf{x})$ and the averaged instability coefficient. As the averaged instability coefficient increases, the reconstruction error exhibits a noticeable upward trend. This positive correlation corroborates our hypothesis that the instability amplifies reconstruction errors.

Verification on text-to-image diffusion models. In practical text-to-image diffusion models, significant reconstruction errors can occasionally occur. To verify that these reconstruction errors are still related to the instability coefficient, we performed a correlation analysis between the reconstruction error $\mathcal{R}(\mathbf{x})$ and the expansion coefficient \mathcal{E} on the Stable Diffusion 3.5 model [11]. Detailed experimental settings are provided in the supplementary material.

The experimental results are illustrated in Figure 4(c). It demonstrate that the reconstruction error $\mathcal{R}(\mathbf{x})$ is significantly positively correlated with the averaged instability coefficient \mathcal{E} in Stable Diffusion 3.5. This finding validates our hypothesis that instability contributes to reconstruction inaccuracies in real-world diffusion models. In the supplementary material, we provide more visual examples of reconstruction failure cases.

4 Probabilistic guarantee on the occurrence of instability

In this section, provide theoretical evidence on instability during the ideal diffusion reconstruction process. First, we establish a general probability lower bound without specific assumptions in Section 4.1. For further in-depth analysis, we then discuss the characteristics of the distributions involved in diffusion reconstruction and propose corresponding assumptions in Section 4.2. Finally, based on the distribution assumptions, we provide a theoretical analysis indicating the non-zero probability of instability in Section 4.3.

4.1 Probability lower bound as intuitive evidence for instability

Definition of additional instability metric. Before the formal analysis, we first define *the geometric average of intrinsic instability coefficient* as an indicator of instability.

Definition 4.1 (Geometric average of intrinsic instability coefficient). Suppose $F : \mathbb{R}^n \rightarrow \mathbb{R}^n$ is a continuously differentiable mapping. For any $\mathbf{x} \in \mathbb{R}^n$, we define the *geometric average of intrinsic instability coefficient* as

$$\bar{\mathcal{E}}_F(\mathbf{x}) := \left(\prod_{i=1}^n \mathcal{E}_F(\mathbf{x}, \mathbf{u}_i) \right)^{\frac{1}{n}}, \quad (6)$$

where $\mathbf{u}_1, \dots, \mathbf{u}_n$ is a set of right singular vectors of the Jacobian matrix $J_F(\mathbf{x})$. Note that $\bar{\mathcal{E}}_F(\mathbf{x})$ is also the geometric average of all singular values of F 's Jacobian $J_F(\mathbf{x})$.

When $\bar{\mathcal{E}}_F(\mathbf{x}) > 1$, at least one of $\mathcal{E}_F(\mathbf{x}, \mathbf{u}_i)$ is also greater than one, thereby indicating the instability.

Lower bound of instability's probability. Applying the above instability metric to the diffusion generation mapping G , we can now present the following theorem:

Theorem 4.1 (Probability lower bound of instability). *Suppose G is the ideal diffusion generation mapping defined in Definition 2.1, whose generation distribution is denoted as π_{gen} . Let G^{-1} denote*

its inverse mapping, which represents the ideal diffusion inversion mapping. Further suppose we sample the initial data \mathbf{x} from some underlying real distribution π_{real} for reconstruction. Then, for any $M > 0$, we have

$$\mathcal{P}_M := \pi_{\text{real}}(\{\mathbf{x} : \bar{\mathcal{E}}_G(G^{-1}(\mathbf{x})) > M\}) \geq 1 - \epsilon - \delta, \quad (7)$$

$$\epsilon := \pi_{\text{real}}\left(\left\{\mathbf{x} : p_{\text{gen}}(\mathbf{x}) \geq \frac{1}{(2\pi M^2)^{\frac{n}{2}}} e^{-\frac{2n+3\sqrt{2n}}{2}}\right\}\right), \quad (8)$$

$$\delta := \pi_{\text{real}}(\{\mathbf{x} : \|G^{-1}(\mathbf{x})\|^2 > 2n + 3\sqrt{2n}\}), \quad (9)$$

where $\mathcal{P}_M := \pi_{\text{real}}(\{\mathbf{x} : \bar{\mathcal{E}}_G(G^{-1}(\mathbf{x})) > M\})$ represents the probability of instability in the ideal diffusion reconstruction if $M > 1$, and p_{gen} denotes the probability density function of π_{gen} .

More specifically, \mathcal{P}_M describes the probability that the geometric average of intrinsic instability coefficient $\bar{\mathcal{E}}_G(\mathbf{z})$ is greater than the threshold M on the inverted noise $\mathbf{z} = G^{-1}(\mathbf{x})$, where \mathbf{x} is sampled from the underlying real distribution π_{real} .

Here, ϵ denotes the probability that the density function $p_{\text{gen}}(x)$ of π_{gen} at a real data x greater than a threshold $\frac{1}{(2\pi M^2)^{\frac{n}{2}}} e^{-\frac{2n+3\sqrt{2n}}{2}}$, while δ represents the probability that the inverted noise $G^{-1}(\mathbf{x})$ of a real data significantly deviates from the center. When both ϵ and δ are small enough, and $M > 1$, we can conclude that $\mathcal{P}_M > 0$, and the instability of the diffusion generation mapping is probable to happen during the ideal reconstruction process.

In the next two subsections, we will first make reasonable assumptions based on the characteristics of image data and practical considerations in Section 4.1, and then provide an asymptotic guarantee for the occurrence of instability in Section 4.3.

4.2 Setting discussions for in-depth analysis

To further analyze the probability \mathcal{P}_M of instability during the diffusion reconstruction process, we first need to make reasonable assumptions about the two probability distributions, π_{real} and π_{gen} , involved in Theorem 4.1. In the following sections, we will discuss these two distributions separately.

4.2.1 Discussions on the properties of π_{real} .

The distribution π_{real} represents the distribution of images to be reconstructed and is not constrained by the diffusion model itself. We can assume that any real-world image may be used for reconstruction, so we refer to π_{real} as the *real distribution*.

Based on this analysis and the inherent properties of image data, the real distribution π_{real} is characterized by the following two features:

1. **Support as a cube:** The support of π_{real} is a hypercube in \mathbb{R}^n . After normalization, it can be assumed that $\text{supp}(\pi_{\text{real}}) = [0, 1]^n$. This is because each pixel in an image has bounded values, typically normalized to the interval $[0, 1]$, ensuring that images in n -dimensional space reside within the hypercube $[0, 1]^n$.
2. **Positive minimum density:** The density function p_{real} of π_{real} has a positive minimum value across its support. This implies that every point within $[0, 1]^n$ corresponds to a possible image, including those that may be uncommon or represent noise-like structures. Although such images have extremely low probability density, they remain potential members of π_{real} .

Assumption 4.1 (π_{real} – Support as a cube). The support of π_{real} is the n -dimensional hypercube $[0, 1]^n$, i.e., $\text{supp}(\pi_{\text{real}}) = [0, 1]^n$.

Assumption 4.2 (p_{real} – Each pixel get a chance). The density function p_{real} of π_{real} is continuous on $\text{supp}(\pi_{\text{real}})$, and p_{real} further satisfies $\forall \mathbf{x} \in [0, 1]^n, p_{\text{real}}(\mathbf{x}) \geq C_0 > 0$.

4.2.2 Discussions on the properties of π_{gen} .

The generation distribution π_{gen} refers to the distribution of samples generated by the diffusion model when it starts from Gaussian noises. For complex and high-dimensional image data, π_{gen} typically exhibits sparsity characteristics, meaning it contains several high-probability regions surrounded by areas of lower probability. In theoretical analyses, the mixture of Gaussians is a common choice for

modeling such multi-modal distributions. However, in this work, to better differentiate between high and low probability regions, we construct a more general distribution model named as the *mixture of Gaussian neighbors*. The assumption on the density function p_{gen} of π_{gen} is provided here:

Assumption 4.3 (p_{gen} – Mixture of Gaussian neighbors). The density function p_{gen} can be expressed as $p_{\text{gen}} = \sum_{i=1}^m a_i f_i * g_{w_i}$, where each f_i is a probability density function supported on the open set O_i , $g_{w_i} = \mathcal{N}(0, w_i^2 I)$ is a Gaussian kernel with standard deviation w_i , $*$ denotes convolution operator, $m \in \mathbb{Z}^+$, and the coefficients a_i satisfy $a_i > 0$ for all $i = 1, \dots, m$ and $\sum_{i=1}^m a_i = 1$.

In this density function, each density function f_i on open set O_i captures the high density region, while the convolution with the Gaussian kernel g_{w_i} ensures that the surrounding areas have smoothly decreasing probabilities, and thus models the low density region. This approach allows for a flexible representation of complex, multi-modal distributions commonly encountered in high-dimensional image data. The following theorem further demonstrate the approximation capability of the mixture of Gaussian neighbors.

Theorem 4.2 (Mixture of Gaussian neighbors are Universal Approximators). *The set of density functions $\{p : p = \sum_{i=1}^m a_i f_i * g_{w_i}, f_i \text{ is compactly supported continuous function}\}$ is a dense subset of continuous density function in both L^2 metric [13] and Lévy-Prokhorov metric [4].*

Sparsity assumption group. Combining the model’s actual training process, the meaning of the mixture of Gaussian neighbors can be understood as follows: In high-dimensional space for image data, the training samples is sparse and finite due to the limited capability to collect image. When the model is sufficiently trained on the training set and possesses certain generalization capabilities, it can generate a small neighborhood around each training sample with relatively high probability. Thus, each O_i corresponds to the neighborhood that can be generated around each training sample, and m represents the number of training samples. Considering the sparsity of high-dimensional images and the model’s limited generalization capabilities, we make the following group of assumptions:

Assumption 4.4 (Sparsity assumption group).

1. (Finite training set) We assume that m has an upper bound as the dimension n increases. For convenience, we directly assume that m is a constant.
2. (Sparse data in high-dimensional space) The neighborhoods O_i and O_j do not overlap for any $i \neq j$, and there exists a minimum positive distance $d_{\min} > 0$ between any two distinct neighborhoods O_i and O_j . For convenience, we define $\bar{d}_{\min} := d_{\min} / \sqrt{n}$.
3. (Finite generalization capability) Each neighborhood O_i is included in a hypercube B_i of side length $b_i \ll 1$.
4. (Low probability region) For each f_i , the probability outside its corresponding O_i is upper bounded by a constant $1 - \alpha_i$, i.e., $\int_{O_i^c} f_i * g_{w_i}(\mathbf{x}) d\mathbf{x} < 1 - \alpha_i < 1$.

These assumptions formalize the intuition that in high-dimensional spaces, training samples are finite, sparse, and each training sample can generate a distinct, small neighborhood without overlap. Additionally, the probability density outside these neighborhoods is uniformly bounded, ensuring that low-density regions do not dominate the generation process.

4.3 Asymptotic proof of almost sure instability

Building upon the assumptions on the relevant distributions, in this subsection, we will present a more in-depth asymptotic analysis on \mathcal{P}_M , demonstrating that instability occurs almost surely during diffusion reconstruction when the dimensionality n tends to infinity. Regarding real-world high-dimensional images, this asymptotic result implies that instability will occur with a non-negligible probability within the reconstruction process.

Recall that in Theorem 4.1, we have proved that the instability probability $\mathcal{P}_M \geq 1 - \epsilon - \delta$, where M is the threshold of an instability indicator \mathcal{E}_G defined in Definition 4.1. To prove a almost sure instability as $n \rightarrow \infty$, it is sufficient to prove that $\epsilon \rightarrow 0$ and $\delta \rightarrow 0$ when $M > 1$. Theorem 4.3 exactly supports this claim. The proof is provided in the supplementary material.

Theorem 4.3. *Consider ϵ and δ defined in Equations (8) and (9) in Theorem 4.1. Suppose that Assumptions 4.1 to 4.3 and Assumption 4.4—the sparsity assumption group—hold. When $n \rightarrow \infty$, if M satisfies $M < M_0$, we have*

$$\epsilon := \pi_{\text{real}} \left(\left\{ \mathbf{x} : p_{\text{gen}}(\mathbf{x}) \geq \frac{1}{(2\pi M^2)^{\frac{n}{2}}} e^{-\frac{2n+3\sqrt{2n}}{2}} \right\} \right) \rightarrow 0, \quad (10)$$

$$\delta := \pi_{\text{real}}(\{\mathbf{x} : \|G^{-1}(\mathbf{x})\|^2 > 2n + 3\sqrt{2n}\}) \rightarrow 0, \quad (11)$$

where $M_0 := \min_{1 \leq i \leq m} \exp\left(\frac{1}{8} \frac{d_{\min}^2}{w_i} - \ln \frac{1}{w_i} + 2 + 3\sqrt{\frac{2}{n}}\right) \rightarrow \infty$. Thus, for any fixed $M > 1$, we can conclude that the instability probability $\mathcal{P}_M \rightarrow 1$ as $n \rightarrow \infty$.

The above theorem implies that, for a sufficiently large dimension n , such as the case of high-dimensional image data, the instability probability can be high, significantly greater than zero.

Intuitive explanations. To better understand Theorem 4.3 and the mechanism underlying this highly-probable instability, we revisit the roles of ϵ and δ in the lower bound of the instability probability \mathcal{P}_M . The term $\epsilon := \pi_{\text{real}}\left(\left\{\mathbf{x} : p_{\text{gen}}(\mathbf{x}) \geq \frac{1}{(2\pi M^2)^{\frac{n}{2}}} e^{-\frac{2n+3\sqrt{2n}}{2}}\right\}\right)$ quantifies the probability that samples from π_{real} avoid low probability density regions of π_{gen} . As discussed in Section 4.2, the sparsity of π_{gen} ensures that most regions exhibit negligible probability density, thereby driving ϵ toward zero. Meanwhile, another term $\delta := \pi_{\text{real}}(\{\mathbf{x} : \|G^{-1}(\mathbf{x})\|^2 > 2n + 3\sqrt{2n}\})$ represents the probability that the inverted noise $G^{-1}(\mathbf{x})$ deviates from the Gaussian’s center beyond a squared threshold $2n + 3\sqrt{2n}$ — a bound that scales as infinity when dimensionality n increases. It is known that high-dimensional Gaussian samples in \mathbb{R}^n concentrate near a sphere with squared radius n . This concentration indicates that significant deviations are of small probability, which implies a small δ . Consequently, both two terms can be small, implying a positive instability probability lower bound $1 - \epsilon - \delta$. A detailed derivation is provided in the supplementary material.

5 Related works

The concepts of diffusion inversion and reconstruction were initially introduced by Song et al. [40] as an application of DDIM, and was then used in many image editing tasks [16, 6, 43, 45]. However, many studies have identified limitations in their effectiveness for text-to-image diffusion models, particularly in terms of reconstruction quality [9, 17, 51, 32, 47, 19, 49, 8]. To improve the reconstruction accuracy, some tuning-based methods are proposed to align the re-generation trajectory to the inversion trajectory [32, 10]. As it is recognized that numerical discretization error is the direct cause of reconstruction inaccuracy, high-order ODE solvers for diffusion models offer alternatives to mitigate this issue [30, 31, 22]. Additionally, some works introduce auxiliary variables to ensure the numerical reversibility of the diffusion inversion process [47, 51, 48]. However, it has been noted that such methods can be unstable, as small perturbations in the inverted noise may lead to significant deviations in the reconstructed image [21]. Meanwhile, there remains a lack of comprehensive analysis on the underlying mechanism: why the reconstruction discrepancy can sometimes be sufficiently significant. Different from previous works that proposes new methods, this work attempts to dive into the mechanism and advance the understanding of diffusion models.

6 Conclusion

In this paper, we identify the instability phenomenon as an amplifier on the error observed in diffusion-based image reconstruction. Through rigorous theoretical analysis and comprehensive experimental validations, we demonstrate that instability leads to the amplification of numerical perturbations during the diffusion generation process, thus increasing the reconstruction error. Moreover, we investigate the underlying causes of instability in the diffusion ODE generation process, demonstrating that the inherent sparsity in diffusion generation distribution can cause instability. Meanwhile, we theoretically prove that the instability will almost surely occur during reconstruction for infinite dimensional images. Our work elucidates a critical source of reconstruction inaccuracies. Addressing instability will be essential for advancing the reliability of generative models in practical settings.

Limitations. While our analysis establishes instability in diffusion reconstruction as a principal contributor to significant errors, we do not preclude the coexistence of additional error mechanisms. Furthermore, the probabilistic proof of instability under our realistic assumptions leaves open the formal characterization of necessary and sufficient conditions for instability emergence.

Broader Impacts. This paper aims to advance the understanding on the mechanism of probably large reconstruction error in diffusion models. While this research primarily contributes to the theoretical advancement in the field, it may also inspire future practical improvements and applications, though no immediate societal impacts are identified for specific emphasis at this time.

References

- [1] M. S. Albergo, N. M. Boffi, and E. Vanden-Eijnden. Stochastic interpolants: A unifying framework for flows and diffusions. *arXiv preprint arXiv:2303.08797*, 2023.
- [2] B. D. Anderson. Reverse-time diffusion equation models. *Stochastic Processes and their Applications*, 12(3):313–326, 1982. ISSN 0304-4149. doi: [https://doi.org/10.1016/0304-4149\(82\)90051-5](https://doi.org/10.1016/0304-4149(82)90051-5). URL <https://www.sciencedirect.com/science/article/pii/0304414982900515>.
- [3] Y. Balaji, S. Nah, X. Huang, A. Vahdat, J. Song, Q. Zhang, K. Kreis, M. Aittala, T. Aila, S. Laine, B. Catanzaro, T. Karras, and M.-Y. Liu. eDiff-I: Text-to-image diffusion models with an ensemble of expert denoisers, 2023. URL <https://arxiv.org/abs/2211.01324>.
- [4] P. Billingsley. *Convergence of probability measures*. Wiley Series in Probability and Statistics: Probability and Statistics. John Wiley & Sons Inc., New York, second edition, 1999. ISBN 0-471-19745-9. A Wiley-Interscience Publication.
- [5] Black Forest Labs. Flux.1. <https://blackforestlabs.ai>, 2024. URL <https://blackforestlabs.ai>. Accessed: 2024-12-03.
- [6] H. Chung, B. Sim, D. Ryu, and J. C. Ye. Improving diffusion models for inverse problems using manifold constraints. *NeurIPS*, 35:25683–25696, 2022.
- [7] H. Chung, B. Sim, and J. C. Ye. Come-closer-diffuse-faster: Accelerating conditional diffusion models for inverse problems through stochastic contraction. In *CVPR*, pages 12413–12422, 2022.
- [8] J. Dai, Y. Zhang, S. Chen, J. Yang, and L. Luo. Erddci: Exact reversible diffusion via dual-chain inversion for high-quality image editing. *arXiv preprint arXiv:2410.14247*, 2024.
- [9] P. Dhariwal and A. Nichol. Diffusion models beat GANs on image synthesis. *NeurIPS*, 2021.
- [10] W. Dong, S. Xue, X. Duan, and S. Han. Prompt tuning inversion for text-driven image editing using diffusion models. In *CVPR*, pages 7430–7440, 2023.
- [11] P. Esser, S. Kulal, A. Blattmann, R. Entezari, J. Müller, H. Saini, Y. Levi, D. Lorenz, A. Sauer, F. Boesel, et al. Scaling rectified flow transformers for high-resolution image synthesis. In *ICML*, 2024.
- [12] G. Folland. *Real Analysis: Modern Techniques and Their Applications*. Pure and Applied Mathematics: A Wiley Series of Texts, Monographs and Tracts. Wiley, 2013. ISBN 9781118626399. URL <https://books.google.com.hk/books?id=wI4fAwAAQBAJ>.
- [13] G. B. Folland. *Real analysis: modern techniques and their applications*, volume 40. John Wiley & Sons, 1999.
- [14] Franzen, R. Kodak lossless true color image suite. <http://r0k.us/graphics/kodak>, 1999. URL <http://r0k.us/graphics/kodak>. Accessed: 2024-12-03.
- [15] R. Gal, Y. Alaluf, Y. Atzmon, O. Patashnik, A. H. Bermano, G. Chechik, and D. Cohen-Or. An image is worth one word: Personalizing text-to-image generation using textual inversion. *arXiv preprint arXiv:2208.01618*, 2022.
- [16] A. Hertz, R. Mokady, J. Tenenbaum, K. Aberman, Y. Pritch, and D. Cohen-Or. Prompt-to-prompt image editing with cross attention control. *arXiv preprint arXiv:2208.01626*, 2022.
- [17] J. Ho and T. Salimans. Classifier-free diffusion guidance. *arXiv preprint arXiv:2207.12598*, 2022.
- [18] J. Ho, A. Jain, and P. Abbeel. Denoising diffusion probabilistic models. In *NeurIPS*, 2020.
- [19] S. Hong, K. Lee, S. Y. Jeon, H. Bae, and S. Y. Chun. On exact inversion of dpm-solvers. In *CVPR*, 2024.

- [20] N. Ikeda and S. Watanabe. *Stochastic Differential Equations and Diffusion Processes*. North-Holland Mathematical Library. North Holland, 2014. ISBN 9781483296159. URL <https://books.google.com.hk/books?id=QZb0BQAAQBAJ>.
- [21] X. Ju, A. Zeng, Y. Bian, S. Liu, and Q. Xu. Pnp inversion: Boosting diffusion-based editing with 3 lines of code. In *ICLR*, 2024.
- [22] T. Karras, M. Aittala, T. Aila, and S. Laine. Elucidating the design space of diffusion-based generative models. *arXiv preprint arXiv:2206.00364*, 2022.
- [23] B. Kawar, S. Zada, O. Lang, O. Tov, H. Chang, T. Dekel, I. Mosseri, and M. Irani. Imagic: Text-based real image editing with diffusion models, 2023. URL <https://arxiv.org/abs/2210.09276>.
- [24] Y. Li, H. Wang, Q. Jin, J. Hu, P. Chemerys, Y. Fu, Y. Wang, S. Tulyakov, and J. Ren. Snapfusion: Text-to-image diffusion model on mobile devices within two seconds, 2023. URL <https://arxiv.org/abs/2306.00980>.
- [25] H. Lin, M. Wang, J. Wang, W. An, Y. Chen, Y. Liu, F. Tian, G. Dai, J. Wang, and Q. Wang. Schedule your edit: A simple yet effective diffusion noise schedule for image editing. *arXiv preprint arXiv:2410.18756*, 2024.
- [26] T.-Y. Lin, M. Maire, S. Belongie, J. Hays, P. Perona, D. Ramanan, P. Dollár, and C. L. Zitnick. Microsoft coco: Common objects in context. In *ECCV*, pages 740–755. Springer, 2014.
- [27] Y. Lipman, R. T. Chen, H. Ben-Hamu, M. Nickel, and M. Le. Flow matching for generative modeling. In *ICLR*, 2023.
- [28] X. Liu, C. Gong, and Q. Liu. Flow straight and fast: Learning to generate and transfer data with rectified flow. In *ICLR*, 2023.
- [29] X. Liu, X. Zhang, J. Ma, J. Peng, and Q. Liu. InstafLOW: One step is enough for high-quality diffusion-based text-to-image generation, 2024. URL <https://arxiv.org/abs/2309.06380>.
- [30] C. Lu, Y. Zhou, F. Bao, J. Chen, C. Li, and J. Zhu. Dpm-solver: A fast ode solver for diffusion probabilistic model sampling in around 10 steps. *arXiv preprint arXiv:2206.00927*, 2022.
- [31] C. Lu, Y. Zhou, F. Bao, J. Chen, C. Li, and J. Zhu. Dpm-solver++: Fast solver for guided sampling of diffusion probabilistic models. *arXiv preprint arXiv:2211.01095*, 2022.
- [32] R. Mokady, A. Hertz, K. Aberman, Y. Pritch, and D. Cohen-Or. Null-text inversion for editing real images using guided diffusion models. In *CVPR*, pages 6038–6047, 2023.
- [33] W. Peebles and S. Xie. Scalable diffusion models with transformers. In *ICCV*, pages 4195–4205, 2023.
- [34] P. Pernias, D. Rampas, M. L. Richter, C. J. Pal, and M. Aubreville. Wuerstchen: An efficient architecture for large-scale text-to-image diffusion models, 2023. URL <https://arxiv.org/abs/2306.00637>.
- [35] D. Podell, Z. English, K. Lacey, A. Blattmann, T. Dockhorn, J. Müller, J. Penna, and R. Rombach. Sdxl: improving latent diffusion models for high-resolution image synthesis. *arXiv preprint arXiv:2307.01952*, 2023.
- [36] A. Ramesh, P. Dhariwal, A. Nichol, C. Chu, and M. Chen. Hierarchical text-conditional image generation with clip latents. *arXiv preprint arXiv:2204.06125*, 2022.
- [37] R. Rombach, A. Blattmann, D. Lorenz, P. Esser, and B. Ommer. High-resolution image synthesis with latent diffusion models. In *CVPR*, 2022.
- [38] C. Saharia, W. Chan, S. Saxena, L. Li, J. Whang, E. Denton, S. K. S. Ghasemipour, B. K. Ayan, S. S. Mahdavi, R. G. Lopes, et al. Photorealistic text-to-image diffusion models with deep language understanding. *arXiv preprint arXiv:2205.11487*, 2022.

- [39] R. Schneider. *Convex Bodies: The Brunn-Minkowski Theory*. Encyclopedia of Mathematics and its Applications. Cambridge University Press, 1993. ISBN 9780521352208. URL <https://books.google.com.hk/books?id=2QhT8UCKx2kC>.
- [40] J. Song, C. Meng, and S. Ermon. Denoising diffusion implicit models. *arXiv preprint arXiv:2010.02502*, 2020.
- [41] Y. Song, J. Sohl-Dickstein, D. P. Kingma, A. Kumar, S. Ermon, and B. Poole. Score-based generative modeling through stochastic differential equations. *ICLR*, 2021.
- [42] E. Stein and R. Shakarchi. *Fourier Analysis: An Introduction*. Princeton University Press, 2003. ISBN 9780691113845. URL <https://books.google.com.hk/books?id=I6CJngEACAAJ>.
- [43] X. Su, J. Song, C. Meng, and S. Ermon. Dual diffusion implicit bridges for image-to-image translation. *arXiv preprint arXiv:2203.08382*, 2022.
- [44] T. Tao. *An Introduction to Measure Theory*. Graduate Studies in Mathematics. American Mathematical Society, 2021. ISBN 9781470466404. URL <https://books.google.com.hk/books?id=k0lDEAAAQBAJ>.
- [45] N. Tumanyan, M. Geyer, S. Bagon, and T. Dekel. Plug-and-play diffusion features for text-driven image-to-image translation. In *CVPR*, pages 1921–1930, 2023.
- [46] P. von Platen, S. Patil, A. Lozhkov, P. Cuenca, N. Lambert, K. Rasul, M. Davaadorj, D. Nair, S. Paul, W. Berman, Y. Xu, S. Liu, and T. Wolf. Diffusers: State-of-the-art diffusion models. <https://github.com/huggingface/diffusers>, 2022.
- [47] B. Wallace, A. Gokul, and N. Naik. Edict: Exact diffusion inversion via coupled transformations. In *CVPR*, pages 22532–22541, 2023.
- [48] F. Wang, H. Yin, Y. Dong, H. Zhu, C. Zhang, H. Zhao, H. Qian, and C. Li. Belm: Bidirectional explicit linear multi-step sampler for exact inversion in diffusion models. *arXiv preprint arXiv:2410.07273*, 2024.
- [49] F. Wang, H. Yin, Y.-J. Dong, H. Zhu, H. Zhao, H. Qian, C. Li, et al. Belm: Bidirectional explicit linear multi-step sampler for exact inversion in diffusion models. *NeurIPS*, 2025.
- [50] J. Xiao, R. Feng, H. Zhang, Z. Liu, Z. Yang, Y. Zhu, X. Fu, K. Zhu, Y. Liu, and Z.-J. Zha. Dreamclean: Restoring clean image using deep diffusion prior. In *ICLR*, 2024.
- [51] G. Zhang, J. P. Lewis, and W. B. Kleijn. Exact diffusion inversion via bidirectional integration approximation. In *ECCV*, pages 19–36. Springer, 2024.

Contents of Appendix

A Pseudocode for diffusion reconstruction	1
B Additional experiments	1
B.1 Reconstruction error amplification verified by second-order ODE solver	1
C Discussions on the implication of instability	2
D Detailed proofs	2
D.1 Proof of Proposition 2.1	2
D.2 Proof of Theorem 3.1	3
D.3 Proof of Theorem 4.1	4
D.4 Proof of Theorem 4.1	6
D.4.1 Definition of Lévy-Prokhorov metric	6
D.4.2 Proof of Theorem 4.2	6
D.5 Proof of Theorem 4.3	8
E Experimental settings	11
E.1 Experiments on numerical cases	11
E.2 Experiments on text-to-image diffusion models	12
F Additional reconstructed images	12
G Licenses of used datasets	12

A Pseudocode for diffusion reconstruction

Algorithm 1 Diffusion reconstruction

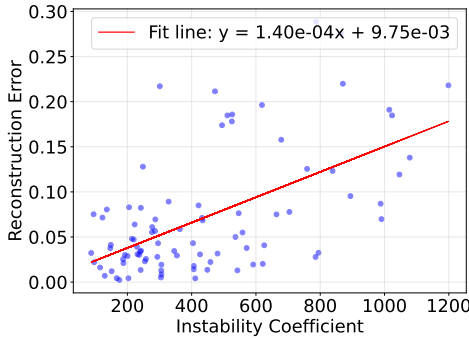
Input: Initial data \mathbf{x} , PF-ODE vector field \mathbf{v} , ODE solver ODESolver
Output: Reconstructed data $\hat{\mathbf{x}}$
 # ODESolver gets four arguments as below
 # ODESolver(initial value, derivative function, initial time, end time)

Diffusion inversion from $t = 0$ to $t = 1$
 1: $\hat{\mathbf{z}} \leftarrow \text{ODESolver}(\mathbf{x}, \mathbf{v}, 0, 1)$
 # Diffusion regeneration from $t = 1$ to $t = 0$
 2: $\hat{\mathbf{x}} \leftarrow \text{ODESolver}(\hat{\mathbf{z}}, \mathbf{v}, 1, 0)$

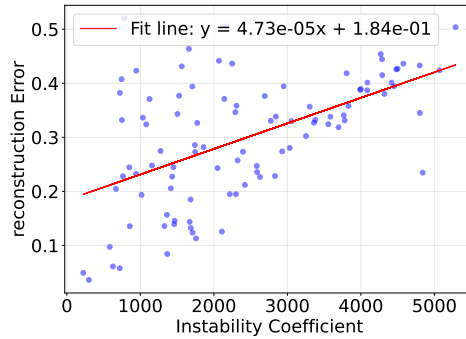
To further illustrate the PF-ODE-based diffusion reconstruction procedure, we provide the pseudocode in Algorithm 1. The pseudocode demonstrates the core logic of the reconstruction process, utilizing an ODE solver that could be any numerical method.

B Additional experiments

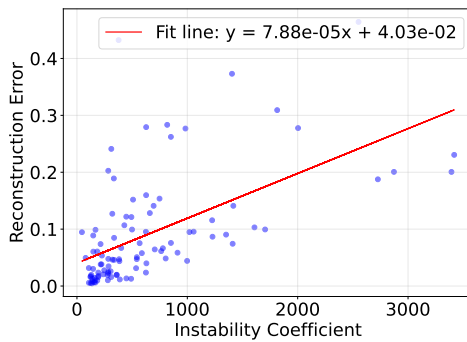
B.1 Reconstruction error amplification verified by second-order ODE solver



(a) Stable Diffusion 3.5 Medium [11]



(b) Stable Diffusion 3.5 Large [11]



(c) FLUX [5]

Figure A1: **Positive correlation between the reconstruction error and instability coefficient verified by second-order Heun ODE solver.** All of the three text-to-image diffusion models exhibit such positive correlation. Experimental details can be found in Appendix E.

In Section 3.2, we have already demonstrated the positive correlation between the reconstruction error and the instability coefficient of diffusion generation mapping. Both the numerical example and the results of Stable Diffusion 3.5 Medium [11] in Figure 4 imply that the occurrence of instability can amplify the reconstruction error. Note that the Euler solver is adopted in Section 3.2.

Here we further emphasize that **this positive correlation between the reconstruction error and the instability coefficient is an inherent property of PF-ODE, and does not rely on specific numerical method.** To support this, we provide more experimental evidence under the second-order Heun ODE solver, rather than the first-order Euler solver in Section 3.2. The results are illustrated in Figure A1. Here we choose three popular different text-to-image diffusion models—Stable Diffusion 3.5 Medium / Large [11] and FLUX [5]. It can be observed that the positive correlation between the reconstruction error and the instability coefficient again appears in all of these three models.

C Discussions on the implication of instability

Our findings reveal that diffusion generation process can exhibit instability when reconstructing a target data, such as image. Specifically, the reconstructed result may vary dramatically under tiny perturbations on the inverted noise, indicating a high sensitivity that undermines the ability to consistently reproduce the original sample. This behavior sheds light on an important limitation of diffusion models’ generalization capability. While diffusion models are often lauded for their strong performance in generating realistic samples, the observed instability implies that they may not have fully learned the underlying structure of the data distribution.

From a theoretical perspective, as discussed in Section 4, such instability can be attributed to the sparsity of the generation distribution: the generation distribution concentrates its probability mass on scattered, small regions in the high-dimensional space, failing to provide robust coverage over the broader data manifold. And this sparsity highlights the model’s limited capacity to generalize beyond the concentrated regions. These insights underscore the need for further research into improving how diffusion models capture the global data distribution, mitigate distributional sparsity, and enhance the stability of their generation process. By addressing these issues, future advancements can potentially expand the scope and reliability of diffusion-based generative models.

D Detailed proofs

D.1 Proof of Proposition 2.1

For convenience, we first repeat Proposition 2.1 to be proved here.

Proposition 2.1 (Instability effect). *Suppose $F : \mathbb{R}^n \rightarrow \mathbb{R}^n$ is a continuously differentiable mapping. For any $\mathbf{x}, \mathbf{u} \in \mathbb{R}^n$, and any $\Delta > 0$, there exists a non-zero perturbation $\mathbf{n} \in \mathbb{R}^n$ such that*

$$\mathcal{A}_F(\mathbf{x}, \mathbf{n}) := \frac{\|F(\mathbf{x} + \mathbf{n}) - F(\mathbf{x})\|}{\|\mathbf{n}\|} \geq \frac{\mathcal{E}_F(\mathbf{x}, \mathbf{u})}{1 + \Delta}, \quad (3)$$

where $\mathcal{A}_F(\mathbf{x}, \mathbf{n})$ is referred to as the instability coefficient. Furthermore, if $\mathcal{E}_F(\mathbf{x}, \mathbf{u}) > 1$, we have a \mathbf{n} that satisfies $\mathcal{A}_F(\mathbf{x}, \mathbf{n}) > 1$, then we say that F exhibits the instability at \mathbf{x} under perturbation \mathbf{n} .

Proof. Given that the operator norm of the Jacobian matrix $J_F(\mathbf{x})$ satisfies $\|J_F(\mathbf{x})\| = \sup_{\mathbf{u}' \in \mathbb{R}^n} \frac{\|J_F(\mathbf{x})\mathbf{u}'\|}{\|\mathbf{u}'\|} \geq \mathcal{E}_F(\mathbf{x}, \mathbf{u})$ for any $\mathbf{x}, \mathbf{u} \in \mathbb{R}^n$, there exists a unit vector \mathbf{h} such that

$$\|J_F(\mathbf{x})\mathbf{h}\| \geq \mathcal{E}_F(\mathbf{x}, \mathbf{u}). \quad (A1)$$

Let $\mathbf{n}_t = t\mathbf{h}$, we have

$$F(\mathbf{x} + \mathbf{n}_t) - F(\mathbf{x}) = J_F(\mathbf{x})\mathbf{n}_t + R(\mathbf{n}_t), \quad (A2)$$

where $R(\mathbf{n}_t)$ is the remainder. Then $\mathcal{A}_F(\mathbf{x}, \mathbf{n}_t)$ is bounded below by:

$$\mathcal{A}_F(\mathbf{x}, \mathbf{n}_t) := \frac{\|F(\mathbf{x} + \mathbf{n}_t) - F(\mathbf{x})\|}{\|\mathbf{n}_t\|} \quad (A3)$$

$$\geq \frac{\|J_F(\mathbf{x})\mathbf{n}_t\| - \|R(\mathbf{n}_t)\|}{\|\mathbf{n}_t\|} \quad (A4)$$

$$\geq \frac{t\mathcal{E}_F(\mathbf{x}, \mathbf{u}) - \|R(\mathbf{n}_t)\|}{\|\mathbf{n}_t\|} \quad (A5)$$

$$= \mathcal{E}_F(\mathbf{x}, \mathbf{u}) - \frac{\|R(\mathbf{n}_t)\|}{\|\mathbf{n}_t\|}, \quad (A6)$$

where the first \geq is by triangle inequality, and the second \geq is by Equation (A1).

Since F is differentiable, the remainder $R(\mathbf{n}_t)$ satisfies $\lim_{t \rightarrow 0} \frac{\|R(\mathbf{n}_t)\|}{\|\mathbf{n}_t\|} = 0$. Then for $\epsilon = \frac{\Delta}{1+\Delta} \mathcal{E}_F(\mathbf{x}, \mathbf{u})$, there exist $\delta > 0$ and $t \leq \delta$ such that $\frac{\|R(\mathbf{n}_t)\|}{\|\mathbf{n}_t\|} \leq \epsilon$, and this can lead to the conclusion

$$\frac{\|F(\mathbf{x} + \mathbf{n}_t) - F(\mathbf{x})\|}{\|\mathbf{n}_t\|} \geq \mathcal{E}_F(\mathbf{x}, \mathbf{u}) - \frac{\|R(\mathbf{n}_t)\|}{\|\mathbf{n}_t\|} \geq \frac{\mathcal{E}_F(\mathbf{x}, \mathbf{u})}{1 + \Delta}. \quad (\text{A7})$$

Furthermore, by the arbitrariness of Δ , when $\mathcal{E}_F(\mathbf{x}, \mathbf{u}) > 1$, there always exists a Δ satisfies $\mathcal{E}_F(\mathbf{x}, \mathbf{u}) > 1 + \Delta$. Thus $\mathcal{A}_F(\mathbf{x}, \mathbf{n}_t) \geq \frac{\mathcal{E}_F(\mathbf{x}, \mathbf{u})}{1+\Delta} > 1$. \square

D.2 Proof of Theorem 3.1

For convenience, we first repeat Theorem 3.1 to be proved here.

Theorem 3.1 (Risk of large reconstruction error). *For any data sample $\mathbf{x} \in \mathbb{R}^n$, consider the diffusion reconstruction process consisting of a numerically approximated diffusion inversion under Euler method and a precise diffusion generation process G . Let $\hat{\mathbf{z}}$ denote the numerically inverted noise, \mathbf{z} denote the ideal inverted noise, and $\hat{\mathbf{x}}$ denote the reconstructed data. Suppose $\mathcal{E}_G(\mathbf{z}', \hat{\mathbf{z}} - \mathbf{z}) > C$ for some $C > 0$ and all $\mathbf{z}' \in \{t\mathbf{z} + (1-t)\hat{\mathbf{z}} : t \in [0, 1]\}$. Then, the upper bound \mathcal{U} of reconstruction error $\mathcal{R}(\mathbf{x})$ satisfies:*

$$\mathcal{U} \geq \underbrace{hM_2 \frac{(C-1)}{2 \log C}}_{\text{Numerical error in inverted noise}} \cdot \underbrace{C}_{\text{Instability amplification}}, \quad (\text{5})$$

where h represents the step size in the numerical solution, and M_2 is the estimated upper bound term for the local truncation error of the Euler method.

Proof. The reconstruction process involves two sequential steps. First, the probability flow ODE in Equation (1) is integrated forward from $t = 0$ to $t = 1$ using the Euler method, yielding the noise corresponding to the image. Then, the same ODE is integrated backward from $t = 1$ to $t = 0$, starting from the noise, to recover the reconstructed image. We use the reconstruction process to evaluate the Lipschitz constant of $\mathbf{v}(\mathbf{x}, t)$ and to analyze the error between the inversion and reconstruction procedures. The form of the probability flow ODE solved using the Euler method in the inversion process is:

$$\mathbf{x}_{t_{n+1}} = \mathbf{x}_{t_n} + (t_{n+1} - t_n)\mathbf{v}(\mathbf{x}_{t_n}, t_n). \quad (\text{A8})$$

The error analysis of Euler's numerical solution involves the estimation of local truncation error (LTE) and global truncation error (GTE), which together determine the method's overall accuracy.

The local truncation error measures the error introduced in a single step of the Euler method. Denoting the time step $t_{n+1} - t_n$ as h , by expanding the true solution $\mathbf{x}(t)$ at time t_{n+1} using a Taylor series around t_n , we obtain:

$$\mathbf{x}(t_{n+1}) = \mathbf{x}(t_n) + h\mathbf{x}'(t_n) + \frac{h^2}{2}\mathbf{x}''(\xi), \quad (\text{A9})$$

where $\xi \in [t_n, t_{n+1}]$. Since $\mathbf{x}'(t_n) = \mathbf{v}(\mathbf{x}_{t_n}, t_n)$, the local truncation error is given by assuming $\mathbf{x}_{t_n} = \mathbf{x}(t_n)$:

$$\text{LTE} := \mathbf{x}(t_{n+1}) - \mathbf{x}_{t_{n+1}} = \frac{h^2}{2}\mathbf{x}''(\xi). \quad (\text{A10})$$

If the second derivative of \mathbf{x} is bounded, that is, $|\mathbf{x}''| \leq M_2$, then the error bound is

$$\text{LTE} \leq \frac{1}{2}M_2h^2. \quad (\text{A11})$$

The global truncation error measures the accumulated error over multiple steps, and the total error can be estimated by summing up the contributions from each step. Let L denote the Lipschitz constant of \mathbf{v} , then the global truncation error E_n satisfies the following recurrence relation:

$$E_{n+1} := \|\mathbf{x}_{t_{n+1}} - \mathbf{x}(t_{n+1})\| \quad (\text{A12})$$

$$= \|(\mathbf{x}_{t_n} + h\mathbf{v}(\mathbf{x}_{t_n}, t_n) - (\mathbf{x}(t_n) + h\mathbf{x}'(t_n) + \frac{h^2}{2}\mathbf{x}''(\xi)))\| \quad (\text{A13})$$

$$\leq \|\mathbf{x}_{t_n} - \mathbf{x}(t_n)\| + h\|\mathbf{v}(\mathbf{x}_{t_n}, t_n) - \mathbf{v}(\mathbf{x}(t_n), t_n)\| + LTE \quad (\text{A14})$$

$$\leq E_n + hL \cdot E_n + \frac{1}{2}M_2h^2. \quad (\text{A15})$$

This yields

$$E_n \leq \frac{hM_2}{2L} (e^L - 1). \quad (\text{A16})$$

While considering the Gronwall inequality for the precise generation process, we can obtain that for two PF-ODE solutions $\mathbf{x}_t, \mathbf{y}_t$ with distinct initial conditions $\mathbf{x}_1, \mathbf{y}_1$ at time $t = 1$, the exact solutions at time $t = 0$ satisfy the following property:

$$\|\mathbf{y}_0 - \mathbf{x}_0\| \leq \|\mathbf{x}_1 - \mathbf{y}_1\|e^L. \quad (\text{A17})$$

This equation will give a upper bound to the intrinsic instability coefficient $\mathcal{E}_G(\mathbf{x}, \mathbf{u})$:

$$\sup_{\mathbf{x}, \mathbf{u}} \mathcal{E}_G(\mathbf{x}, \mathbf{u}) \leq e^L. \quad (\text{A18})$$

From Equation (A18) and the assumption $\mathcal{E}_G(\mathbf{z}', \hat{\mathbf{z}} - \mathbf{z}) > C$, we can infer that $L \geq \log C$. Substituting into our previous discussion on the global truncation error, we have:

$$\mathcal{U} \geq \frac{hM_2}{2L}(e^L - 1) \cdot C \geq hM_2 \frac{C - 1}{2 \log C} \cdot C. \quad (\text{A19})$$

□

D.3 Proof of Theorem 4.1

To prove Theorem 4.1, we first present two lemmas.

Lemma D.1. *For any ODE with a unique solution:*

$$\frac{d\mathbf{x}_t}{dt} = \mathbf{v}(\mathbf{x}_t, t), \quad (\text{A20})$$

its solution can be expressed as $\mathbf{x}_t = \phi_t(\mathbf{x}_0)$ for $t \in [0, 1]$ with the initial condition \mathbf{x}_0 at $t = 0$. Let $p_t(\mathbf{x})$ be a probability density function that satisfies $\int_{\phi_t^{-1}(A)} p_0(\mathbf{x})d\mathbf{x} = \int_A p_t(\mathbf{x})d\mathbf{x}$ for any measurable set A . Then the geometric average of intrinsic instability coefficient for mapping ϕ_1 , i.e., $\bar{\mathcal{E}}_{\phi_1}(\mathbf{x})$ defined as Definition 4.1, satisfies:

$$|\bar{\mathcal{E}}_{\phi_1}(\mathbf{x})|^n \geq \exp\left(\int_0^1 \nabla \cdot \mathbf{v}(\mathbf{x}_t, t)dt\right) = \frac{p_0(\mathbf{x})}{p_1(\phi_1(\mathbf{x}))},$$

Proof. For any $t \in [0, 1]$ and \mathbf{x}_0 , define $J(t) = \frac{\partial \mathbf{x}_t}{\partial \mathbf{x}_0}$, where \mathbf{x}_t is defined in Equation (A20). Then $J(0) = I$, $J(1) = J_{\phi_1}(\mathbf{x}_0)$, and

$$\frac{d}{dt}J(t) = \frac{d}{dt} \frac{\partial \mathbf{x}_t}{\partial \mathbf{x}_0} \quad (\text{A21})$$

$$= \frac{\partial \mathbf{v}(\mathbf{x}_t, t)}{\partial \mathbf{x}_0} \quad (\text{A22})$$

$$= \frac{\partial \mathbf{v}(\mathbf{x}_t, t)}{\partial \mathbf{x}_t} \circ J(t). \quad (\text{A23})$$

Multiplying $J^{-1}(t)$ in both sides, we have

$$\frac{dJ(t)}{dt} \circ J^{-1}(t) = \frac{\partial \mathbf{v}(\mathbf{x}_t, t)}{\partial \mathbf{x}_t}. \quad (\text{A24})$$

Denote the i -th eigenvalue of $J(t)$ as $\lambda_i(J(t))$. With Equation (A24), we can obtain $\frac{d}{dt} \log |\prod_{i=1}^n \lambda_i(J(t))|$ as follows

$$\frac{d}{dt} \log \left| \prod_{i=1}^n \lambda_i(J(t)) \right| = \sum_{i=1}^n \frac{d}{dt} \log |\lambda_i(J(t))| \quad (\text{A25})$$

$$= \sum_{i=1}^n \frac{d\lambda_i(J(t))}{dt} \lambda_i(J(t))^{-1} \quad (\text{A26})$$

$$= \text{tr} \left(\frac{dJ(t)}{dt} \circ J^{-1}(t) \right) \quad (\text{A27})$$

$$= \text{tr} \left(\frac{\partial \mathbf{v}(\mathbf{x}_t, t)}{\partial \mathbf{x}_t} \right) \quad (\text{A28})$$

$$= \nabla \cdot \mathbf{v}(\mathbf{x}_t, t). \quad (\text{A29})$$

Thus deduce that

$$\log \left| \prod_{i=1}^n \lambda_i(J(t)) \right| = \int_0^1 \nabla \cdot \mathbf{v}(\mathbf{x}_t, t) dt. \quad (\text{A30})$$

On the other hand, for the probability density we can derive that:

$$\frac{d \log p_t(\mathbf{x}_t)}{dt} = \nabla \log p_t(\mathbf{x}_t) \cdot \frac{d\mathbf{x}_t}{dt} + \frac{\partial}{\partial t} \log p_t(\mathbf{x}, t) \quad (\text{A31})$$

$$= \nabla \log p_t(\mathbf{x}_t) \cdot \mathbf{v}(\mathbf{x}_t, t) + \frac{\partial}{\partial t} \log p_t(\mathbf{x}, t) \quad (\text{A32})$$

$$= \frac{\nabla p_t(\mathbf{x}_t)}{p_t(\mathbf{x}_t)} \cdot \mathbf{v}(\mathbf{x}_t, t) - \frac{\nabla \cdot (p_t(\mathbf{x}_t) \mathbf{v}(\mathbf{x}_t, t))}{p_t(\mathbf{x}_t)} \quad (\text{A33})$$

$$= -\nabla \cdot \mathbf{v}(\mathbf{x}_t, t), \quad (\text{A34})$$

where Equation (A33) is a result from Fokker-Planck equation: $\frac{\partial p_t(\mathbf{x}_t)}{\partial t} = -\nabla \cdot (p_t(\mathbf{x}_t) \mathbf{v}(\mathbf{x}_t, t))$. Thus we conclude that

$$\log p_t(\mathbf{x}_t) + \log \left| \prod_{i=1}^n \lambda_i(J(t)) \right| = \log p_0(\mathbf{x}_0) + \log \left| \prod_{i=1}^n \lambda_i(J(0)) \right|. \quad (\text{A35})$$

Note that $J(0)$ is the identity matrix, hence we obtain

$$|\bar{\mathcal{E}}_{\phi_1}(\mathbf{x})|^n \geq \left| \prod_{i=1}^n \lambda_i(J(t)) \right| = \frac{p_0(\mathbf{x}_0)}{p_t(\mathbf{x}_t)}, \quad (\text{A36})$$

where the first inequality holds because the product of the singular values of a matrix is greater than the absolute value of the product of its eigenvalues. \square

Lemma D.2. Let γ be the standard Gaussian probability density function and G^{-1} be the inversion function. For all $\mathbf{x} \in \text{supp}(\pi_{\text{data}})$, and for all $K > 0, k > 0$, we have

$$\begin{aligned} \pi_{\text{real}} \left(\left\{ \mathbf{x} : \frac{p_{\text{data}}(\mathbf{x})}{\gamma(G^{-1}(\mathbf{x}))} < K \right\} \right) &\geq \pi_{\text{real}} (\{\mathbf{x} : p_{\text{data}}(\mathbf{x}) < kK\}) \\ &- \pi_{\text{real}} (\{\mathbf{x} : \gamma(G^{-1}(\mathbf{x})) \leq k\}). \end{aligned} \quad (\text{A37})$$

Proof.

$$\pi_{\text{real}} \left(\left\{ \mathbf{x} : \frac{p_{\text{data}}(\mathbf{x})}{\gamma(G^{-1}(\mathbf{x}))} < K \right\} \right) \quad (\text{A38})$$

$$= \pi_{\text{real}} (\{\mathbf{x} : p_{\text{data}}(\mathbf{x}) < K\gamma(G^{-1}(\mathbf{x}))\} \cap \{\mathbf{x} : \gamma(G^{-1}(\mathbf{x})) > k\}) \quad (\text{A39})$$

$$+ \pi_{\text{real}} (\{\mathbf{x} : p_{\text{data}}(\mathbf{x}) < K\gamma(G^{-1}(\mathbf{x}))\} \cap \{\mathbf{x} : \gamma(G^{-1}(\mathbf{x})) \leq k\}) \quad (\text{A39})$$

$$\geq \pi_{\text{real}} (\{\mathbf{x} : p_{\text{data}}(\mathbf{x}) < K\gamma(G^{-1}(\mathbf{x}))\} \cap \{\mathbf{x} : \gamma(G^{-1}(\mathbf{x})) > k\}) \quad (\text{A40})$$

$$\geq \pi_{\text{real}} (\{\mathbf{x} : \gamma(G^{-1}(\mathbf{x})) > k\} \cap \{\mathbf{x} : p_{\text{data}}(\mathbf{x}) < kK\}) \quad (\text{A41})$$

$$\geq \pi_{\text{real}} (\{\mathbf{x} : p_{\text{data}}(\mathbf{x}) < kK\}) - \pi_{\text{real}} (\{\mathbf{x} : \gamma(G^{-1}(\mathbf{x})) \leq k\}). \quad (\text{A42})$$

\square

Now the conclusion of Theorem 4.1 is a direct corollary of the two lemmas above. For convenience, we first repeat Theorem 4.1 to be proved here.

Theorem 4.1 (Probability lower bound of instability). *Suppose G is the ideal diffusion generation mapping defined in Definition 2.1, whose generation distribution is denoted as π_{gen} . Let G^{-1} denote its inverse mapping, which represents the ideal diffusion inversion mapping. Further suppose we sample the initial data \mathbf{x} from some underlying real distribution π_{real} for reconstruction. Then, for any $M > 0$, we have*

$$\mathcal{P}_M := \pi_{\text{real}}(\{\mathbf{x} : \bar{\mathcal{E}}_G(G^{-1}(\mathbf{x})) > M\}) \geq 1 - \epsilon - \delta, \quad (7)$$

$$\epsilon := \pi_{\text{real}}\left(\left\{\mathbf{x} : p_{\text{gen}}(\mathbf{x}) \geq \frac{1}{(2\pi M^2)^{\frac{n}{2}}} e^{-\frac{2n+3\sqrt{2n}}{2}}\right\}\right), \quad (8)$$

$$\delta := \pi_{\text{real}}(\{\mathbf{x} : \|G^{-1}(\mathbf{x})\|^2 > 2n + 3\sqrt{2n}\}), \quad (9)$$

where $\mathcal{P}_M := \pi_{\text{real}}(\{\mathbf{x} : \bar{\mathcal{E}}_G(G^{-1}(\mathbf{x})) > M\})$ represents the probability of instability in the ideal diffusion reconstruction if $M > 1$, and p_{gen} denotes the probability density function of π_{gen} .

More specifically, \mathcal{P}_M describes the probability that the geometric average of intrinsic instability coefficient $\bar{\mathcal{E}}_G(\mathbf{z})$ is greater than the threshold M on the inverted noise $\mathbf{z} = G^{-1}(\mathbf{x})$, where \mathbf{x} is sampled from the underlying real distribution π_{real} .

Proof. From Lemma D.1 and Lemma D.2, we have

$$\mathcal{P}_M = \pi_{\text{real}}(\{\mathbf{x} : \bar{\mathcal{E}}_G(G^{-1}(\mathbf{x})) > M\}) \quad (\text{A43})$$

$$\geq \pi_{\text{real}}\left(\left\{\mathbf{x} : \frac{p_{\text{gen}}(\mathbf{x})}{\gamma(G^{-1}(\mathbf{x}))} < M^{-n}\right\}\right) \quad (\text{A44})$$

$$\geq \pi_{\text{real}}\left(\left\{\mathbf{x} : p_{\text{gen}}(\mathbf{x}) < \frac{1}{(2\pi M^2)^{\frac{n}{2}}} e^{-\frac{2n+3\sqrt{2n}}{2}}\right\}\right) \\ - \pi_{\text{real}}\left(\left\{\mathbf{x} : \gamma(G^{-1}(\mathbf{x})) < \frac{1}{(2\pi)^{\frac{n}{2}}} e^{-\frac{2n+3\sqrt{2n}}{2}}\right\}\right), \quad (\text{A45})$$

where the first inequality Equation (A44) follows from Lemma D.1 if we take p_0 as the Gaussian density function γ and p_t as the density of generated distribution p_{gen} during the generation process, the second inequality Equation (A45) follows from Lemma D.2 with $k = \frac{1}{(2\pi)^{\frac{n}{2}}} e^{-\frac{2n+3\sqrt{2n}}{2}}$. \square

D.4 Proof of Theorem 4.1

Before the formal proof of Theorem 4.1, we first provide the definition of Lévy-Prokhorov metric [4].

D.4.1 Definition of Lévy-Prokhorov metric

Definition D.1 (Lévy-Prokhorov metric). For a subset $A \subset \mathbb{R}^n$, define the ϵ -neighborhood of A by

$$A^\epsilon := \{p \in \mathbb{R}^n : \exists q \in A, d(p, q) < \epsilon\} = \bigcup_{p \in A} B_\epsilon(p). \quad (\text{A46})$$

where $B_\epsilon(p)$ is the open ball of radius ϵ centered at p . Let $\mathcal{P}(\mathbb{R}^n)$ denotes the collection of all probability measures on \mathbb{R}^n . The Lévy-Prokhorov metric $\pi : \mathcal{P}(\mathbb{R}^n)^2 \rightarrow [0, +\infty)$ is defined as follows:

$$\pi(\mu, \nu) := \inf\{\epsilon > 0 : \mu(A) \leq \nu(A^\epsilon) + \epsilon \text{ and } \nu(A) \leq \mu(A^\epsilon) + \epsilon\}. \quad (\text{A47})$$

This metric is equivalent to weak convergence of measures [4].

D.4.2 Proof of Theorem 4.2

For convenience, we first repeat Theorem 4.2 to be proved here.

Theorem 4.2 (Mixture of Gaussian neighbors are Universal Approximators). *The set of density functions $\{p : p = \sum_{i=1}^m a_i f_i * g_{w_i}, f_i \text{ is compactly supported continuous function}\}$ is a dense subset of continuous density function in both L^2 metric [13] and Lévy-Prokhorov metric [4].*

Proof. n -dimensional Hermite functions form a complete orthogonal basis of $L^2(\mathbb{R}^n)$ space [42]. Hermite functions can be expressed as:

$$\phi_\alpha(\mathbf{x}) = H_\alpha(\mathbf{x})e^{-\|\mathbf{x}\|^2}. \quad (\text{A48})$$

Here α is a multi-index, an ordered n -tuple of nonnegative integers. $H_\alpha(\mathbf{x})$ is a polynomial of α order called Hermite polynomials. By Plancherel theorem, the Fourier transform is an isomorphism on $L^2(\mathbb{R}^n)$. [12] It is sufficient to prove the Fourier transform of $\{p(\mathbf{x}) = \sum_{i=1}^m a_i f_i * g_{w_i}(\mathbf{x})\}$ can converge to Hermite functions in L^2 . We denote the Fourier transform of any function h as \widehat{h} , with the wide hat notation $\widehat{\cdot}$. Thus

$$\sum_{i=1}^m a_i \widehat{f_i * g_{w_i}}(\mathbf{x}) = \sum_{i=1}^m a_i \widehat{f_i} \cdot e^{-\frac{1}{2}w_i^2\|\mathbf{x}\|^2}. \quad (\text{A49})$$

Since the continuous compact support function $C_c(\mathbb{R}^n)$ is dense in $L^2(\mathbb{R}^n)$ [12], by the isomorphism, $\{a_i \widehat{f_i}\}$ is also dense in $L^2(\mathbb{R}^n)$. $H_\alpha(\mathbf{x})e^{-\frac{1}{2}\|\mathbf{x}\|^2}$ is a L^2 function. Then we derive that $\forall \phi_\alpha, \forall \delta > 0, \exists a, f$ and take $w_i = 1$,

$$\|\widehat{af * g_1}(\mathbf{x}) - \phi_\alpha(\mathbf{x})\|_{L^2} = \|(H_\alpha(\mathbf{x})e^{-\frac{1}{2}\|\mathbf{x}\|^2} - a\widehat{f})e^{-\frac{1}{2}\|\mathbf{x}\|^2}\|_{L^2} \quad (\text{A50})$$

$$\leq \|(H_\alpha(w_i\mathbf{x})e^{-\frac{1}{2}\|\mathbf{x}\|^2} - a\widehat{f})\|_{L^2} \|e^{-\frac{1}{2}\|\mathbf{x}\|^2}\|_{L^\infty} \quad (\text{A51})$$

$$\leq \delta. \quad (\text{A52})$$

The first inequality is Hölder's inequality, and the second inequality follows from the density of a, f in the L^2 space. $\forall \epsilon > 0, h(x) \in L^2(\mathbb{R}^n)$, there exists a finite set of multi-index $\{\alpha_k, k \leq N\}$ and sequence $\{\theta_{\alpha_k}\}$ such that

$$\left\| \sum_{k \leq N} \theta_{\alpha_k} \phi_{\alpha_k}(\mathbf{x}) - \widehat{h}(\mathbf{x}) \right\|_{L^2} \leq \frac{\epsilon}{2}, \quad (\text{A53})$$

then for each ϕ_{α_k} choose a $a_{\alpha_k} f_{\alpha_k} * g_{w_{\alpha_k}}$ such that $\|a_{\alpha_k} f_{\alpha_k} * g_{w_{\alpha_k}}(\mathbf{x}) - \theta_{\alpha_k} \phi_{\alpha_k}(\mathbf{x})\|_{L^2} \leq \frac{\epsilon}{2N}$, we obtain that

$$\left\| \sum_{k \leq N} a_{\alpha_k} f_{\alpha_k} * g_{w_{\alpha_k}}(\mathbf{x}) - \widehat{h}(\mathbf{x}) \right\|_{L^2} \quad (\text{A54})$$

$$\leq \left\| \sum_{k \leq N} a_{\alpha_k} f_{\alpha_k} * g_{w_{\alpha_k}}(\mathbf{x}) - \sum_{k \leq N} \theta_{\alpha_k} \phi_{\alpha_k}(\mathbf{x}) \right\|_{L^2} + \left\| \sum_{k \leq N} \theta_{\alpha_k} \phi_{\alpha_k}(\mathbf{x}) - \widehat{h}(\mathbf{x}) \right\|_{L^2} \quad (\text{A55})$$

$$\leq \epsilon, \quad (\text{A56})$$

which shows the density of $\sum_{k \leq N} a_i f_i * g_{w_i}$ in $L^2(\mathbb{R})$. Now we prove the density in Lévy-Prokhorov metric, $\forall f$ is a density function of $\mathbb{R}^n, \forall \epsilon > 0$, we can construct an ϵ -decomposition as follow: Since f is integrable, there is a compact set K_f in \mathbb{R} with $\int_{K_f^c} f(x)dx < \epsilon$ and $\int_{\partial K_f} f(x)dx = 0$. The interior of K is an open set O and by the structure theorem of open sets, there exists a decomposition $O = \bigcup_i O_i, \{O_i\}$ are disjoint open sets and to make the index set finite, the distance between O_i is no less than some $d > 0$. Then we have $O = \bigcup_{i \leq N'} O_i$

Then we define $a_i := \int_{O_i} f(\mathbf{x})d\mathbf{x}$ and $f_i(\mathbf{x}) := \frac{1}{a_i} f(\mathbf{x})I_{O_i}, \forall A' \subset \bigcup_{i \leq N'} O_i$, denote $A' \cap O_j$ as A'_j

$$\int_{A'} |f - \sum_i a_i f_i * g_{w_i}| d\mathbf{x} \quad (\text{A57})$$

$$= \sum_j \int_{A'_j} |f - \sum_i a_i f_i * g_{w_i}| d\mathbf{x} \quad (\text{A58})$$

$$\leq \sum_j \int_{A'_j} |f - a_j f_j * g_{w_j}| d\mathbf{x} + \sum_j \int_{A'_j} |a_j f_j * g_{w_j} - \sum_i a_i f_i * g_{w_i}| d\mathbf{x}. \quad (\text{A59})$$

g_{w_j} is an approximate identity about w_j and when w_j is sufficiently small, $\int_{A'_j} |f - a_j f_j * g_{w_j}| d\mathbf{x} \leq \|f - a_j f_j * g_{w_j}\|_{L^1} \leq \frac{\epsilon}{2N'}$ and

$$\int_{A'_i} |a_j f_j * g_{w_j} - \sum_i a_i f_i * g_{w_i}| d\mathbf{x} = \sum_{i \neq j} \int_{A'_i} |a_i f_i * g_{w_i}| d\mathbf{x} \leq \sum_{i \neq j} \frac{1}{2\pi w_i} \exp(-\frac{d^2}{2w_i^2}), \quad (\text{A60})$$

when w_i is sufficiently small, $\sum_{i \neq j} \frac{1}{2\pi w_i} \exp(-\frac{d^2}{2w_i^2}) \leq \frac{\epsilon}{2N'}$. From this we conclude that $\forall A' \subset \bigcup_{i \leq N'} O_i$, we have

$$\int_{A'} f(\mathbf{x}) d\mathbf{x} \leq \int_{A'} \sum_i a_i f_i * g_{w_i}(\mathbf{x}) d\mathbf{x} + \epsilon, \quad (\text{A61})$$

$$\int_{A'} \sum_i a_i f_i * g_{w_i}(\mathbf{x}) d\mathbf{x} \leq \int_{A'} f(\mathbf{x}) d\mathbf{x} + \epsilon. \quad (\text{A62})$$

And $\forall A' \subset O^c$, $\int_{A'} f(\mathbf{x}) d\mathbf{x} \leq \epsilon$, then it is sufficient to prove

$$\int_{A'} \sum_i a_i f_i * g_{w_i}(\mathbf{x}) d\mathbf{x} \leq \int_{A'^c} f(\mathbf{x}) d\mathbf{x} + \epsilon \quad (\text{A63})$$

and this could also be obtained by the L^1 convergence property of approximate identity: $\int_{A'} \sum_i a_i f_i * g_{w_i}(\mathbf{x}) d\mathbf{x} < \epsilon$ with appropriate w_i .

In summary, $\forall A' \subset \mathbb{R}^n$,

$$\int_{A'} f(\mathbf{x}) d\mathbf{x} = \int_{A' \cap O} f(\mathbf{x}) d\mathbf{x} + \int_{A' \cap O^c} f(\mathbf{x}) d\mathbf{x} \quad (\text{A64})$$

$$\leq \int_{(A' \cap O)^\epsilon} \sum_i a_i f_i * g_{w_i}(\mathbf{x}) d\mathbf{x} + \epsilon + \epsilon \quad (\text{A65})$$

$$\leq \int_{(A')^{2\epsilon}} \sum_i a_i f_i * g_{w_i}(\mathbf{x}) d\mathbf{x} + 2\epsilon, \quad (\text{A66})$$

$$\int_{A'} \sum_i a_i f_i * g_{w_i}(\mathbf{x}) d\mathbf{x} = \int_{A' \cap O} \sum_i a_i f_i * g_{w_i}(\mathbf{x}) d\mathbf{x} + \int_{A' \cap O^c} \sum_i a_i f_i * g_{w_i}(\mathbf{x}) d\mathbf{x} \quad (\text{A67})$$

$$\leq \int_{(A' \cap O)^\epsilon} f(\mathbf{x}) d\mathbf{x} + \epsilon + \epsilon \quad (\text{A68})$$

$$\leq \int_{(A')^{2\epsilon}} f(\mathbf{x}) d\mathbf{x} + 2\epsilon. \quad (\text{A69})$$

By the arbitrariness of ϵ , we conclude that the set of distributions with probability density function $\{\sum_i a_i f_i * g_{w_i}\}$ is dense. \square

D.5 Proof of Theorem 4.3

For convenience, we first repeat Theorem 4.3 to be proved here.

Theorem 4.3. Consider ϵ and δ defined in Equations (8) and (9) in Theorem 4.1. Suppose that Assumptions 4.1 to 4.3 and Assumption 4.4—the sparsity assumption group—hold. When $n \rightarrow \infty$, if M satisfies $M < M_0$, we have

$$\epsilon := \pi_{\text{real}} \left(\left\{ \mathbf{x} : p_{\text{gen}}(\mathbf{x}) \geq \frac{1}{(2\pi M^2)^{\frac{n}{2}}} e^{-\frac{2n+3\sqrt{2n}}{2}} \right\} \right) \rightarrow 0, \quad (10)$$

$$\delta := \pi_{\text{real}}(\{\mathbf{x} : \|G^{-1}(\mathbf{x})\|^2 > 2n + 3\sqrt{2n}\}) \rightarrow 0, \quad (11)$$

where $M_0 := \min_{1 \leq i \leq m} \exp\left(\frac{1}{8} \frac{d_{\min}^2}{w_i} - \ln \frac{1}{w_i} + 2 + 3\sqrt{\frac{2}{n}}\right) \rightarrow \infty$. Thus, for any fixed $M > 1$, we can conclude that the instability probability $\mathcal{P}_M \rightarrow 1$ as $n \rightarrow \infty$.

Proof. The overall idea of the proof is to find a value M related to w_i such that as $n \rightarrow \infty$, we have $w_i \rightarrow 0$, thereby implying that both ϵ and δ tend to 0 and $M \rightarrow \infty$. From Assumption 4.3

$$p_{\text{gen}}(\mathbf{x}) = \sum_{i=1}^m \int_{\mathbb{R}^n} a_i f_i(\mathbf{y}) g_{w_i}(\mathbf{x} - \mathbf{y}) d\mathbf{y} \quad (\text{A70})$$

$$= \sum_{i=1}^m \int_{\bigcup_{i \leq m} O_i} a_i f_i(\mathbf{y}) \frac{1}{(2\pi w_i^2)^{\frac{n}{2}}} e^{-\frac{\|\mathbf{x}-\mathbf{y}\|^2}{2w_i^2}} d\mathbf{y} \quad (\text{A71})$$

$$\leq \sum_{i=1}^m \int_{\bigcup_{i \leq m} O_i} a_i f_i(y) \frac{1}{(2\pi w_i^2)^{\frac{n}{2}}} e^{-\frac{\min_{i \leq m} d(\mathbf{x}, O_i)^2}{2w_i^2}} d\mathbf{y} \quad (\text{A72})$$

$$= \sum_{i=1}^m a_i \frac{1}{(2\pi w_i^2)^{\frac{n}{2}}} e^{-\frac{\min_{i \leq m} d(\mathbf{x}, O_i)^2}{2w_i^2}} \quad (\text{A73})$$

$$\leq \max_{i \leq m} \left\{ \frac{1}{(2\pi w_i^2)^{\frac{n}{2}}} e^{-\frac{\min_{i \leq m} d(\mathbf{x}, O_i)^2}{2w_i^2}} \right\}. \quad (\text{A74})$$

We define a dominating function

$$h_{w_1, \dots, w_m}(\mathbf{x}) := \max_{i \leq m} \left\{ \frac{1}{(2\pi w_i^2)^{\frac{n}{2}}} e^{-\frac{\min_{i \leq m} d(\mathbf{x}, O_i)^2}{2w_i^2}} \right\}, \quad (\text{A75})$$

which is monotonically decreasing about $\min_{i \leq m} d(\mathbf{x}, O_i)$ and can be written as $h_{w_1, \dots, w_m}(\mathbf{x}) = h'_{w_1, \dots, w_m}(\min_{i \leq m} d(\mathbf{x}, O_i))$, where $h'_{w_1, \dots, w_m}(x) := \max_{i \leq m} \left\{ \frac{1}{(2\pi w_i^2)^{\frac{n}{2}}} e^{-\frac{x^2}{2w_i^2}} \right\}$. From the above inequality we obtain:

$$\left\{ \mathbf{x} : p_{\text{gen}}(\mathbf{x}) \geq \frac{1}{(2\pi M^2)^{\frac{n}{2}}} e^{-\frac{2n+3\sqrt{2n}}{2}} \right\} \quad (\text{A76})$$

$$\subset \left\{ \mathbf{x} : h_{w_1, \dots, w_m}(\mathbf{x}) \geq \frac{1}{(2\pi M^2)^{\frac{n}{2}}} e^{-\frac{2n+3\sqrt{2n}}{2}} \right\} \quad (\text{A77})$$

$$= \left\{ \mathbf{x} : \min_{i \leq m} d(\mathbf{x}, O_i) \leq r_M \right\}, \quad (\text{A78})$$

where

$$r_M := \left\| h'_{w_1, \dots, w_m} \left(\frac{1}{(2\pi M^2)^{\frac{n}{2}}} e^{-\frac{2n+3\sqrt{2n}}{2}} \right) \right\|. \quad (\text{A79})$$

Based on this, taking $M \leq M_0 := \min_{1 \leq i \leq m} \exp\left(\frac{1}{8} \frac{\bar{d}_{\min}^2}{w_i} - \ln \frac{1}{w_i} + 2 + 3\sqrt{\frac{2}{n}}\right)$, we observe that $M_0 \rightarrow \infty$ as $w_i \rightarrow 0$, and in the following part we will proof $w_i \rightarrow 0$ as $n \rightarrow \infty$. Here \bar{d}_{\min} is the minimum of distance between B_i .

Since h'_{w_1, \dots, w_m} is radial, once M is fixed, r_M is well defined. Thus there exists a unique w_j in Equation (A75) such that for any \mathbf{x} satisfying $\min_{i \leq m} d(\mathbf{x}, O_i) = r_M$, we have

$$h_{w_1, \dots, w_m}(\mathbf{x}) = \frac{1}{(2\pi w_j^2)^{\frac{n}{2}}} e^{-\frac{\min_{i \leq m} d(\mathbf{x}, O_i)^2}{2w_j^2}}. \quad (\text{A80})$$

Then from Equation (A78) we deduce that

$$\left\{ \mathbf{x} : p_{\text{gen}}(\mathbf{x}) \geq \frac{1}{(2\pi M^2)^{\frac{n}{2}}} e^{-\frac{2n+3\sqrt{2n}}{2}} \right\} \quad (\text{A81})$$

$$\subset \left\{ \min_{i \leq m} d(\mathbf{x}, O_i) \leq \frac{1}{2} \sqrt{nw_j} \bar{d}_{\min} \right\} = \bigcup_{i \leq m} \left\{ d(\mathbf{x}, O_i) \leq \frac{1}{2} \sqrt{nw_j} \bar{d}_{\min} \right\}, \quad (\text{A82})$$

where \bar{d}_{\min} is the dimension-normalized d_{\min} , as defined in Assumption 4.4. As we discussed previously in the third of Assumption 4.4, all O_i is contained by a cube B_i , consequently $\left\{ d(\mathbf{x}, O_i) \leq \frac{1}{2} \sqrt{nw_j} \bar{d}_{\min} \right\} \subset \left\{ d(\mathbf{x}, B_i) \leq \frac{1}{2} \sqrt{nw_j} \bar{d}_{\min} \right\}$ and to calculate the Lebesgue measure of the geometric body obtained by expanding an n -dimensional cube B_i outward by a distance $\frac{1}{2} \sqrt{nw_j} \bar{d}_{\min}$, we can utilize the Steiner formula [39], which expresses the volume as the sum of the expansion volumes of different-dimensional faces of the original cube, with each expanded volume contribution being the product of the corresponding ball volume.

For each $k \leq n$, the number of k -dimensional faces is $\binom{n}{k} \cdot 2^{n-k}$ and each has a expansion volume contribution $b_i^k \cdot \omega_{n-k} \left(\frac{1}{2} \sqrt{nw_j} \bar{d}_{\min}\right)^{n-k} \left(\frac{1}{2}\right)^{n-k}$. Based on this, we conclude that

$$m \left\{ d(\mathbf{x}, B_i) \leq \frac{1}{2} \sqrt{nw_j} \bar{d}_{\min} \right\} = \sum_{k=0}^n \binom{n}{k} b_i^k \cdot \omega_{n-k} \left(\frac{1}{2} \sqrt{nw_j} \bar{d}_{\min}\right)^{n-k}. \quad (\text{A83})$$

Comparing with the support of π_{real} , which contain some disjoint cubes centered at x_i and the edge length is no less than $\sqrt{3\pi eb_i}$, we can make the following analysis:

$$\frac{m \{d(\mathbf{x}, O_i) \leq \frac{1}{2}\sqrt{nw_j \bar{d}_{\min}}\}}{(\sqrt{3\pi eb_i})^n} \leq \frac{\pi^{\frac{n}{2}} (b_i \sqrt{n} + \frac{1}{2}\sqrt{nw_j \bar{d}_{\min}})^n}{\Gamma(\frac{n}{2} + 1)(\sqrt{3\pi eb_i})^n} \quad (\text{A84})$$

$$\sim \frac{\pi^{\frac{n}{2}}}{\sqrt{\pi n} (\frac{n}{2e})^{\frac{n}{2}}} \frac{(b_i \sqrt{n} + \frac{1}{2}\sqrt{nw_j \bar{d}_{\min}})^n}{(\sqrt{3\pi eb_i})^n} \quad (\text{Stirling formula}). \quad (\text{A85})$$

With the low probability region assumption in Assumption 4.4, we have

$$\int_{O_i} f_i * g_{w_i}(\mathbf{x}) d\mathbf{x} \quad (\text{A86})$$

$$\leq \int_{B_i} f_i * g_{w_i}(\mathbf{x}) d\mathbf{x} \quad (\text{A87})$$

$$= \int_{B_i} \int f_i(\mathbf{y}) g_{w_i}(\mathbf{x} - \mathbf{y}) d\mathbf{y} d\mathbf{x} \quad (\text{A88})$$

$$= \int f_i(\mathbf{y}) \int_{B_i} g_{w_i}(\mathbf{x} - \mathbf{y}) d\mathbf{x} d\mathbf{y} \quad (\text{A89})$$

$$\leq \int f_i(\mathbf{y}) \int_{B_i} g_{w_i}(\mathbf{x} - \mathbf{x}_i) d\mathbf{x} d\mathbf{y} \quad (\text{A90})$$

$$= \int_{B_i} g_{w_i}(\mathbf{x} - \mathbf{x}_i) d\mathbf{x} \quad (\text{A91})$$

$$\leq \left(\int_{-b_i}^{b_i} \frac{1}{2\pi w_i^2} e^{-\frac{x^2}{2w_i^2}} dx \right)^n. \quad (\text{A92})$$

As mentioned previously we obtain that $\int_{O_i} f_i * g_{w_i}(\mathbf{x}) d\mathbf{x} > \alpha_i$ leads to w_i converging to zero when $n \rightarrow \infty$, which means $M_0 \rightarrow \infty$. Substituting this result into Equation (A85), we obtain: $\frac{m \{d(\mathbf{x}, O_i) \leq \frac{1}{2}\sqrt{nw_j \bar{d}_{\min}}\}}{(\sqrt{3\pi eb_i})^n}$ converge to 0 as $n \rightarrow \infty$. Thus we can deduce that

$$\lim_{n \rightarrow \infty} \frac{m \left\{ \bigcup_{i \leq m} \left\{ d(\mathbf{x}, O_i) \leq \frac{1}{2}\sqrt{nw_j \bar{d}_{\min}} \right\} \right\}}{m \{ \text{supp}(\pi_{\text{real}}) \}} = 0. \quad (\text{A93})$$

See π_{real} on \mathbb{R}^n as taking finite pixels from a continuous function $f \in C(S)$ representing a infinitely precise real image. S is a compact subset of \mathbb{R}^2 . The pixels form a finite ϵ -dense set S_n of the separable space S . And $S_\infty = \bigcup_{n=1}^{\infty} S_n$ is a countable dense set of S . And all the continuous function on S_∞ is $C(S)$. $\bigcup_n \mathcal{B}(\mathbb{R}^n)$ forms a semialgebra with a premeasure that generates $\mathcal{B}(C(S))$. With the Kolmogorov extension theorem [44], there is a unique distribution π_{real}' on $\mathcal{B}(C(S))$ generated by all $\pi_{\text{real}}^{(n)}$ on \mathbb{R}^n . Additionally, considering that step functions could uniformly converge to any $f \in C(S)$. The finite n-pixel image space can also be seen as step functions on S : $S = \bigcup_{i \leq n} U_i$ is a decomposition of disjoint set, each U_i represent a pixel and $m(U_i) = \frac{m(S)}{n}$. For any $C(S)$ value random variable X , there is a step function value random variable $X_n = \sum_{i \leq n} \mathbf{x}_i I_{U_i}$ as X 's n-dimensional projection and X_n converges to X almost surely in the function space equipped with the uniform norm:

$$P(\omega : \|X_n(\omega) - X(\omega)\| \rightarrow 0) = 1. \quad (\text{A94})$$

From this, we derive the convergence of probability law :

$$P^{X_n} \xrightarrow{w} P^X, \quad (\text{A95})$$

which means $\pi_{\text{real}}^{(n)}$ converge to π_{real}' in the Banach space of continuous and step functions on S with uniform norm [20].

Since $\pi_{\text{real}}^{(n)}$ is absolutely continuous about π_{gen} till the infinite-dimensional case, $\delta' = \pi_{\text{gen}}(G(\mathbf{z}) : \|\mathbf{z}\|^2 \geq 2n + 3\sqrt{2n}) = 1 - F(2n + 3\sqrt{2n}; n)$, where $F(\cdot; n)$ is the cumulative

distribution function of chi-square distribution χ_n^2 and $1 - F(2n + 3\sqrt{2n}; n)$ converges to 0. And the set $B_n = \{\|z\|^2 \geq 2n + 3\sqrt{2n}\}$ when placed in the function space means $\|f_z\|_{L^2} \geq m(S)(2 + 3\sqrt{\frac{2}{n}})$, f_z is the step function associated with z , as a result we obtain $B_n \subset B_{n+1}$, so $B_\infty = \lim_{n \rightarrow \infty} B_n = \bigcup_{n=1}^{\infty} B_n$ and $\lim_{n \rightarrow \infty} \pi_{\text{real}}^{(n)}(B_n) = \pi_{\text{real}}'(B_\infty)$. While $\pi'_{gen}(B_\infty) = \lim_{n \rightarrow \infty} \pi_{gen}(G(\mathbf{z}) : \|z\|^2 \geq 2n + 3\sqrt{2n}) = 0$, we derive that $\lim_{n \rightarrow \infty} \delta = \lim_{n \rightarrow \infty} \pi_{\text{real}}(G(\mathbf{z}) : \|z\|^2 \geq 2n + 3\sqrt{2n}) = \lim_{n \rightarrow \infty} \pi_{\text{real}}^{(n)}(B_n) = 0$.

Using the same analytical approach, we can obtain the ratio of maximum and minimum p_{real} on $\bigcup_{i \leq m} \{d(\mathbf{x}, O_i) \leq \frac{1}{2}\sqrt{nw_j d_{\min}}\}$: $\frac{C}{C_0}$ has some limit value. Combining with Equation (A93), we arrive at the conclusion that

$$\lim_{n \rightarrow \infty} \epsilon = \lim_{n \rightarrow \infty} \pi_{\text{real}} \left(\bigcup_{i \leq m} \left\{ \mathbf{x} : d(\mathbf{x}, O_i) \leq \frac{1}{2}\sqrt{nw_j d_{\min}} \right\} \right) \quad (\text{A96})$$

$$= \lim_{n \rightarrow \infty} \frac{\pi_{\text{real}} \left(\bigcup_{i \leq m} \left\{ \mathbf{x} : d(\mathbf{x}, O_i) \leq \frac{1}{2}\sqrt{nw_j d_{\min}} \right\} \right)}{\pi_{\text{real}}(\text{supp}(\pi_{\text{real}}))} = 0. \quad (\text{A97})$$

□

E Experimental settings

E.1 Experiments on numerical cases

Settings for experiments in Section 3.1 To verify that instability indeed exists in diffusion generation, we conduct experiments on a two-dimensional diffusion model with a mixture of Gaussians as the generation distribution, consisting of three Gaussian components. To compute the intrinsic instability coefficient and obtain the results shown in Figure 3(b), we utilize the finite difference to estimate the intrinsic instability coefficient. The specific steps are as follows:

1. Uniformly sample initial points as on a 201×201 uniform grid of the area $[-1, 1] \times [-1, 1]$. Denote each initial point as $\mathbf{x}[i, j]$, where i denotes the index along x -axis, and j denotes the index along y -axis. Thus, $\mathbf{x}[i, j] = (-1 + \frac{i}{100}, -1 + \frac{j}{100})$ for $i, j = 0, 1, \dots, 200$.
2. Numerically solve the PF-ODE in Equation (1) using the RK45 solver from $t = 1$ to $t = 0$. Each solution at $t = 1$, *i.e.*, the generated sample, can be denoted as $\hat{G}(\mathbf{x}[i, j])$ for each initial point $\mathbf{x}[i, j]$.
3. Estimate the intrinsic instability coefficient as $\mathcal{E}_G(\mathbf{x}[i, j], \mathbf{n}_y) \approx \|\hat{G}(\mathbf{x}[i, j + 1]) - \hat{G}(\mathbf{x}[i, j])\| / \|\mathbf{x}[i, j + 1] - \mathbf{x}[i, j]\|$.

When computing the instability coefficient shown in Figure 3(c), we use two points with larger input difference. The results demonstrate that the obtained instability coefficient is lower bounded by the corresponding intrinsic instability coefficient.

Settings for experiments in Section 3.2 Similarly, we adopt the two-dimensional mixture of Gaussians as the generation distribution for these experiments. To obtain the correlation between reconstruction error and instability coefficient as shown in Figure 4(b), we follow the experimental procedure as below:

1. Uniformly sample initial data from $[-1, 1] \times [-1, 1]$.
2. Compute the reconstructed samples using the diffusion reconstruction process: first obtain the inverted noise $\hat{\mathbf{z}} = \hat{G}^{-1}(\mathbf{x})$ for each initial data \mathbf{x} , and then regenerate the data as $\hat{\mathbf{x}} = \hat{G}(\hat{\mathbf{z}})$.
3. Calculate the reconstruction error $\mathcal{R}(\mathbf{x})$ for each sample.
4. Estimate the intrinsic instability coefficient by 1) applying a small perturbation noise \mathbf{n} to each inverted noise $\hat{\mathbf{z}}$, and then 2) regenerating the data under perturbation as $\tilde{\mathbf{x}} = \hat{G}(\hat{\mathbf{z}} + \mathbf{n})$,

and 3) finally resulting in the estimation of intrinsic instability coefficient as $\mathcal{E}_G(\hat{z}, \frac{\mathbf{n}}{\|\mathbf{n}\|}) \approx \|\tilde{\mathbf{x}} - \hat{\mathbf{x}}\|/\|\mathbf{n}\|$.

5. Statistically analyze the correlation between $\mathcal{R}(\mathbf{x})$ and the intrinsic instability coefficient.

This procedure allows us to empirically assess the relationship between instability coefficients and reconstruction inaccuracies, thereby validating the theoretical insights discussed in Section 3.

E.2 Experiments on text-to-image diffusion models

Model and inference settings. Models used in our experiments include Stable Diffusion 3.5 Medium / Large [11] and FLUX.1-dev [5], accessed via the `diffusers` library [9] under the PyTorch framework. The inference is conducted on NVIDIA A800 GPUs.

During inference, most of the default scheduler configuration parameters are adopted for the numerical solution of the PF ODE. As for the ODE solver, we adopt Euler method following the default setting, except for experiments in Appendix B.1 that the Heun ODE solver is used. Besides, the number of inference steps is adjusted to 500 steps for both diffusion inversion and re-generation. The procedure to obtain the reconstruction error and the intrinsic instability coefficient is similar to that in the numerical experiments. The adopted image dataset is introduced below.

Datasets. The experiments primarily utilize the MSCOCO2014 dataset [26]. For the experiments presented in Figure 4, we randomly select 100 images from the validation set of MSCOCO2014 for diffusion reconstruction. As for experiments in Appendix B.1, we adopt the same sampled images as in Figure 4.

F Additional reconstructed images

To visually demonstrate that images are often difficult to be accurately reconstructed, we present failure cases of reconstruction by Stable Diffusion 3.5 [11]. These images are selected from Kodak24 dataset [14] in Figure A2 and MS-COCO 2014 [26] in Figure A3. For the reconstruction that includes both diffusion inversion and regeneration processes, we follow the default scheduler setting in `diffusers` [46] with null text prompt and 100 inference steps for both inversion and regeneration.

G Licenses of used datasets

We list all the licenses of used datasets, code and models in Table A1.

Table A1: Licenses of datasets, code and models used in the paper.

Name	License
Datasets	
MS-COCO2014 [26]	Creative Commons Attribution 4.0 License
Kodak24 [14]	Free
Code	
Diffusers [46]	Apache License 2.0
Models	
Stable Diffusion 3.5 Medium [11]	Stability AI Community License
Stable Diffusion 3.5 Large [11]	Stability AI Community License
FLUX.1-Dev [5]	FLUX.1 [dev] Non-Commercial License

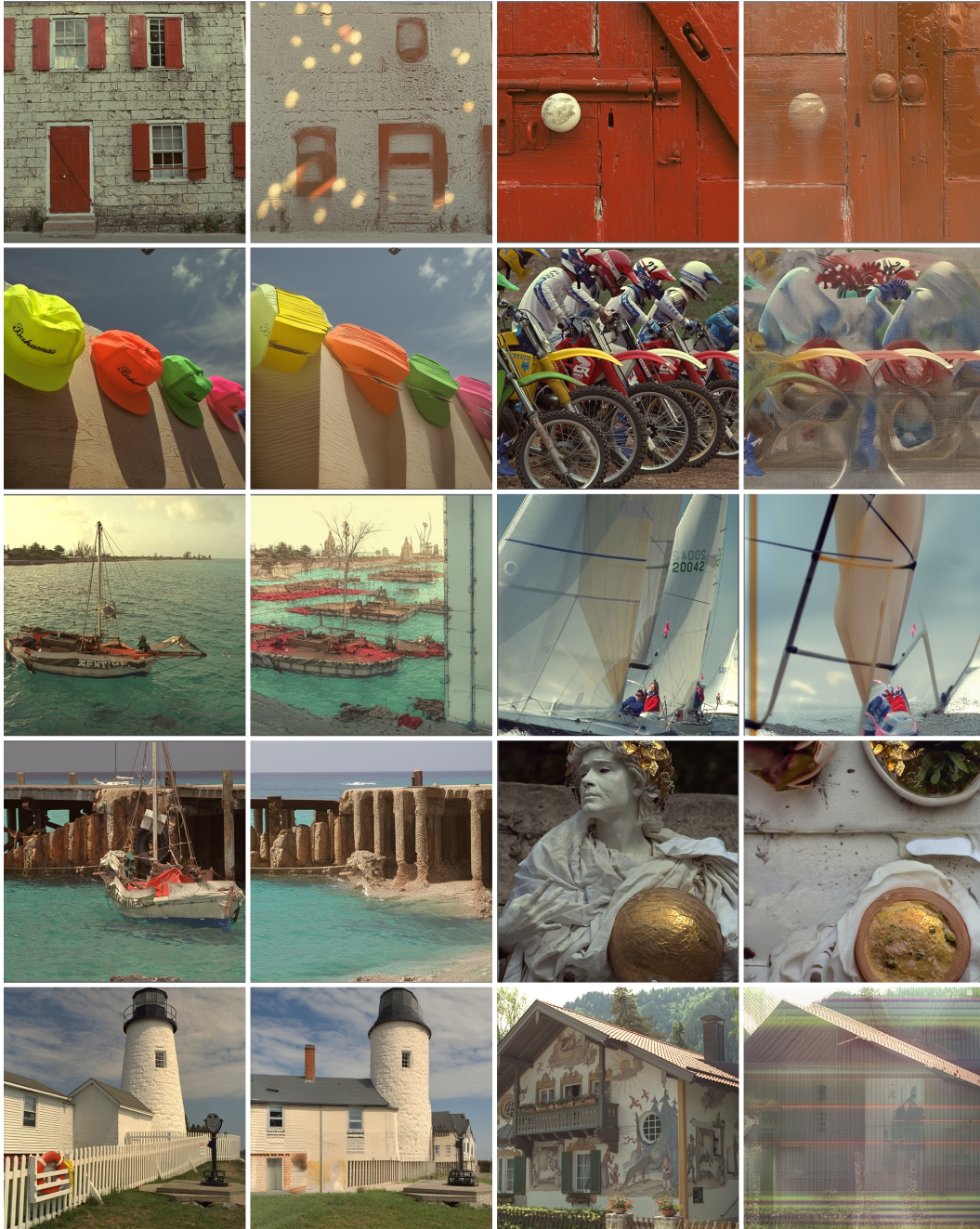


Figure A2: More failure cases of reconstruction on real images from Kodak24 dataset [14] by Stable Diffusion 3.5 [11]. In each row, the first and the third images are original real images, another two images are reconstructed ones.

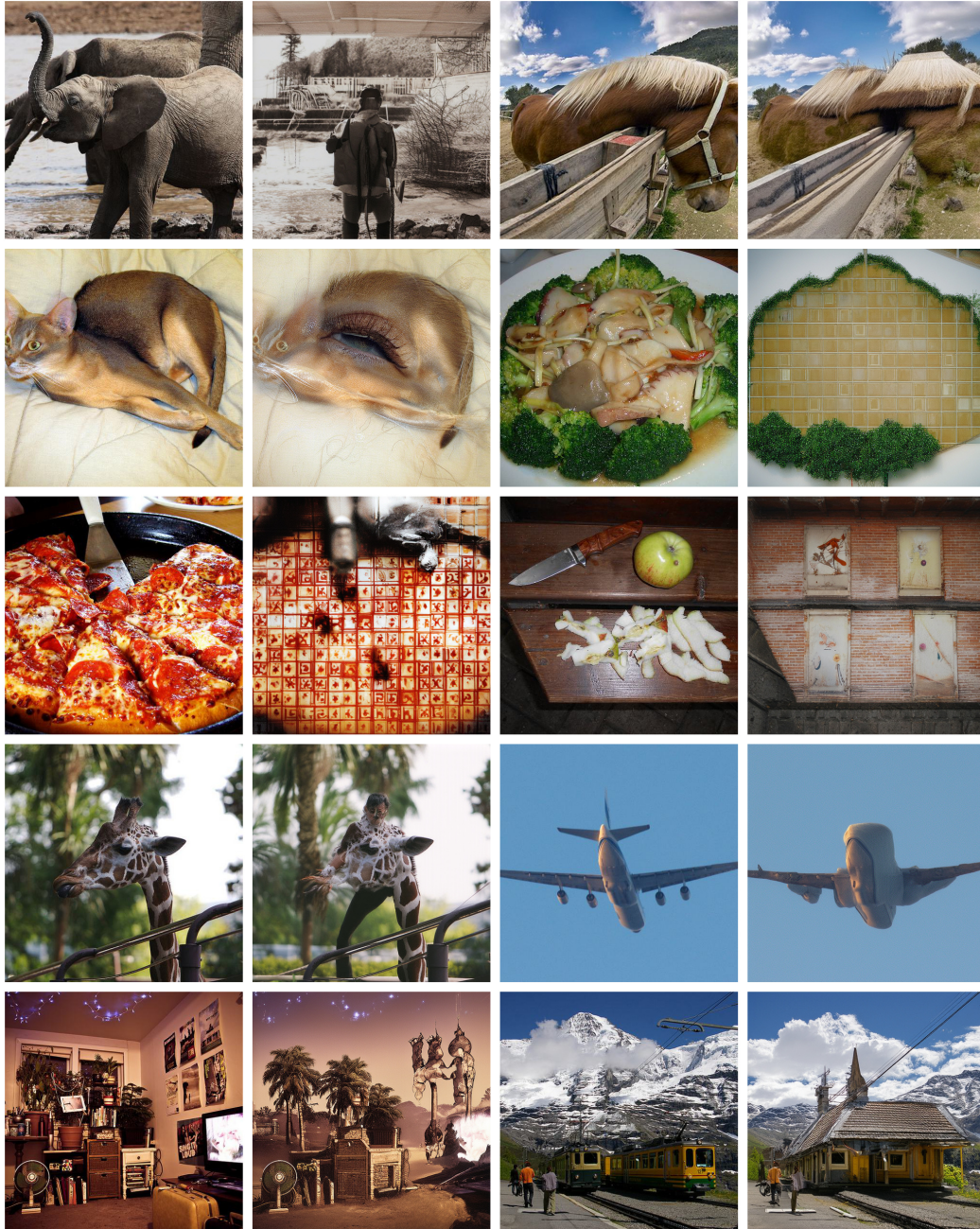


Figure A3: More failure cases of reconstruction on real images from MS-COCO 2014 dataset [26] by Stable Diffusion 3.5 [11]. In each row, the first and the third images are original real images, another two images are reconstructed ones.